THE UNIVERSITY OF CHICAGO

THE PROPAGATION OF FLAME FRONTS THROUGH INHOMOGENEOUSLY MAGNETIZED PLASMA

A DISSERTATION SUBMITTED TO
THE FACULTY OF THE DIVISION OF THE PHYSICAL SCIENCES
IN CANDIDACY FOR THE DEGREE OF
DOCTOR OF PHILOSOPHY

DEPARTMENT OF ASTRONOMY AND ASTROPHYSICS

BY
IAN SCHNEIDER REMMING

CHICAGO, ILLINOIS
AUGUST 2018

Dedicated to my family.

TABLE OF CONTENTS

LIST OF FIGURES

LIST OF TABLES

ACKNOWLEDGMENTS

I thank Professors Fausto Cattaneo, Doyal "Al" Harper, Arieh Konigl, and Robert Rosner for useful suggestions that led to improvements to the text of this dissertation. I also thank Professors Alexei Khokhlov and Fausto Cattaneo for their mentorship. This work was supported by the NSF under grant No. AST-0709181 and by NSF Graduate Research Fellowship under grant Nos. DGE-1144082 and DGE-1746045.

ABSTRACT

The effects of an inhomogeneous magnetic medium on the propagation of magneto-hydrodynamical (MHD) laminar flame fronts are investigated. This investigation is motivated by the occurrence of magnetized thermonuclear combustion in several astrophysical systems. Magnetized thermonuclear burning occurs on the surfaces of neutron stars during Type I X-ray bursts, within the interiors of white dwarfs during Type Ia supernovae, during classical novae, and may be important for certain core collapse supernovae as well. Thermonuclear flames that propagate in these systems travel through inhomogeneous magnetic fields. I present the results of a series of 1.5-dimensional numerical simulations of magnetized flame propagation conducted using the MHD extension to the High Speed Combustion and Detonation (HSCD) code. A simplified flame model is used with one-step Arrhenius kinetics, an ideal gas equation of state, and constant thermal conductivity coefficients. Although idealized, the model allows for the opportunity to study the physics of the problem without the complexities of the nuclear kinetics of thermonuclear burning. Steady-state solutions for this simplified model were presented in Remming & Khokhlov (2016). To confirm that the solutions are indeed steady, as well as to verify the physics algorithms programmed in HSCD, laminar flame solutions are mapped to the HSCD computational grid and evolved in time without being exposed to perturbations. They remain steady on the HSCD grid to a very high degree for long integration times. After this verification step, I simulate the propagation of laminar flames through inhomogeneous magnetic media. A changing magnetic medium significantly alters the structure of the flame through the generation of an electric current that is directed out of the plane of the flame front. The electric current rotates the direction of the magnetic field within the flame and produces strong shear flows. Furthermore, for flames that conduct heat anisotropically and that propagate at an angle $0 < \psi \lesssim \pi/2$ to the magnetic field (where ψ is relative to the flame front normal), the flame speed increases due to the non-uniform magnetic field. Naturally occurring flames in astrophysical systems may experience similar

changes to their structure and speed that would influence the observational properties of these systems.

CHAPTER 1

INTRODUCTION

Laminar flame physics have important applications to astrophysical thermonuclear explosions. A widely established class of Type Ia supernova models predicts that a supernova explosion is triggered by the inception of a subsonic flame or deflagration in the interior of a Chandrashehar mass white dwarf (see Hillebrandt & Niemeyer 2000 for a review of SN Ia explosion models; Reinecke et al. 2002; Gamezo et al. 2003). As the flame front propagates through the white dwarf it is distorted by hydrodynamical instabilities, such as the Rayleigh-Taylor and Kelvin-Helmholtz instabilities, that destroy the laminarity of the flame and lead to turbulence. Nevertheless laminar flame properties like the flame velocity affect the explosion kinematics and composition by, for instance, influencing the efficiency of flame front wrinkling due to the Rayleigh-Taylor instability (Gamezo et al. 2003). Moreover, the plasma through which the flame propagates during a supernova is likely magnetized. In fact, there are reasons to believe that the white dwarf interior can be strongly magnetized (as large as $\gtrsim 10^{12}$ G) (Remming & Khokhlov 2014; henceforth, RK14). Remming & Khokhlov (2016) (henceforth, RK16) studied the physics of steady-state magnetized laminar flames in the context of astrophysical thermonuclear combustion. Flame structure, speed, and thickness were calculated for a wide range of magnetic field strengths and orientations relative to the flame front using idealized and supernova-like physical models. For example, RK16 found that a magnetized flame in a $0.5\mathrm{C}^{12} + 0.5\mathrm{O}^{16}$ by mass fuel mixture with density $\rho = 10^7$ g cm^{-3}, temperature $T = 10^8$ K, and magnetic field strength $H = 3 \times 10^{12}$ G moves at a speed that is up to 2.5 times faster than the non-magnetic flame when the magnetic field is oriented nearly parallel to the flame front. When the density is increased to $\rho = 3 \times 10^9$ g cm^{-3}, the steady-state flame speed is reduced by a factor of about 0.38 relative to the unmagnetized flame. In a recent paper, Hristov et al. (2018) performed three-dimensional magneto-hydrodynamical simulations of flame propagation in an environment resembling a

small inner region of a white dwarf. The authors studied the dependence of the flame physics on the strength and orientation of the initial magnetic field. Among other results, they found that the flame front speed tends to decrease with increasing initial field strength up to about 10^{11} G. When the initial field was set to $\sim 10^{12}$ G, the flame propagated at a speed that was a factor of 3 to 4 above the field-free flame. The authors attributed the increase to the burning speed to smale-scale finger-like features that developed across the flame front during the simulation. During a SN Ia the magnetic field morphology will be complex and may be characterized by non-uniformities in the strength of the field in the white dwarf. How inhomogeneities in a magnetic field affect magnetized flame propagation is the topic of this paper.

Type I X-ray bursts (henceforth, X-ray bursts or bursters) provide another example of a system that undergoes thermonuclear combustion. X-ray bursts occur in binary systems in which there is a neutron star and, typically, a low mass main sequence star or another compact star. In an X-ray bursting binary, mostly hydrogen-rich and/or helium-rich matter is transferred to the neutron star from the atmosphere of the companion star through Roche-lobe overflow. The accreted mass forms a $\sim 10^3 - 10^4$ cm layer of H and He on the surface of the neutron star. This layer of accreted material is gravitationally compressed and heated through the release of its gravitational energy. Further amounts of heat are generated through nuclear burning. In the event that the rate of thermal energy creation overtakes the rate at which the star cools then the accreted layer is thermally unstable and a thermonuclear flash occurs. The flash increases the X-ray flux of the binary system to many times the persistent flux with a total energy for the burst in the range 10^{39}-10^{40} ergs (Galloway et al. 2008, also see references therein). The X-ray burst arises from the thermonuclear combustion of the hydrogen and helium fuel on the surface of the neutron star. In addition to normal Type I X-ray bursts, there is a class of X-ray superbursts. A superburst releases about 10^{42} ergs in the explosion (Cumming & Bildsten 2001, also see references therein). Superbursts are

thought to be triggered by unstable ignition of carbon at a deeper layer in the neutron star than a normal X-ray burst (Cumming & Bildsten 2001).

Magnetic fields may play an important role in X-ray bursts. Of the collection of known thermonuclear bursting neutron stars, five are persistent accretion-powered pulsars (Watts 2012). The pulsar's magnetic field is thought to constrain the accretion flow to move along field lines from the accretion disk toward the neutron star's magnetic pole (Psaltis & Chakrabarty 1999). This creates a surface hot spot that comes into view once per rotation of the star. For example, one well-studied persistent accretion-powered pulsar, SAX J1808.4 - 3658, has an estimated magnetic field strength of $\sim 10^8$ G (Psaltis & Chakrabarty 1999, also see Watts 2012). A magnetic field of this strength may play a dynamically important role during thermonuclear bursts. Cavecchi et al. (2016) performed two-dimensional simulations of neutron star burning fronts propagating through an initially vertical magnetic field. They found that magnetic fields in the range $10^7 - 10^{10}$ G can accelerate the flame, giving rise to a simulated burst rise time closer to what is observed. The material that is accreted onto a neutron star likely brings with it angular momentum. Previous studies have explored how the accreted angular momentum is transported through the neutron star's surface layers (Fujimoto 1993, Piro & Bildsten 2007, and Keek et al. 2009). The accreted angular momentum creates a differentially rotating profile in the neutron star's outer layers. Shearing between layers lead to magnetic field growth and turbulent mixing. In this conceptual framework, the magnetic field growth is understood in the context of the Tayler-Spruit dynamo (Spruit 2002). In their calculations, Piro & Bildsten (2007) and Keek et al. (2009) both find that the magnetic field that is generated has a radial component strength of $\sim 10^5$ G and a toroidal component strength of $\sim 10^{10}$ G. Assuming that this pre-burst turbulent mixing process occurs and that the magnetic field generated persists during the burst, the flame that is born would propagate through an inhomogeneous and dynamically important magnetic field. Moreover, this process can take place in X-ray bursting neutron stars that

are not also persistent pulsars (Piro & Bildsten 2007).

In this paper I consider non-steady idealized flame propagation through inhomogeneous magnetic media. Although actual astrophysical thermonuclear combustion occurs in very non-ideal environments, RK16 found many similarities in the structure and propagation of idealized magnetized laminar flames and fully degenerate and relativisitic magnetized flames. The purpose of this paper is to study the effects of inhomogeneous magnetic fields on flame structure and propagation for idealized conditions. The expectation is that the flame's general behavior as it reacts to the perturbing magnetic field will bear similarities to the corresponding thermonuclear flame's behavior, and, thus, the conclusions of this analysis will provide needed qualitative clues about the behavior of astrophysical thermonuclear flames propagating through inhomogeneous magnetic fields.

The outline for the remainder of this paper is as follows. I set up the problem treated in Chapter 2 with a description of the assumptions taken, the equations solved, and the numerical methods used. I performed reactive flow magneto-hydrodynamics simulations using the High Speed Combustion and Detonation (HSCD) code. To perform MHD simulations with HSCD, I added to the code as a module the third-order accurate WENO finite difference algorithm. To improve the temporal accuracy of HSCD, I added the third-order accurate total variations-diminishing Runge-Kutta algorithm. The implementation of the WENO and Runge-Kutta algorithms is based on Mignone et al. (2010). For this project, I implemented thermal conduction explicitly, and I tracked the conserved chemical quantity through the use of upwinded fluxes. In Chapter 3, I review the physics of magnetized flame propagation and demonstrate that the HSCD code maintains the structure of steady flame solutions mapped onto the code's grid. In Chapter 4, I motivate the setup of the simulations within the context of astrophysical combustion. Chapter 5 presents an analysis of the results of the simulations. Following this in Chapter 6, I provide conclusions and discuss the applicability of the results to astrophysical flames.

CHAPTER 2

THE PROBLEM

2.1 Assumptions and equations

Consider the propagation of one-dimensional magnetized, exothermic reaction fronts or flames (simple description follows Calleja 2006). A sketch illustration of the principal features of a flame front is shown in Figure 2.1. The illustration depicts the four zones that comprise a reaction front. There are the (a) fuel, (b) the heating zone, (c) the reaction zone, and (d) the ashes, also known as the products of burning. The frame of reference moves with the speed of the reaction front, so the fuel enters the reaction front from the left and the ashes exit to the right. As the fuel is burned in the reaction zone energy is released in the form of heat that diffuses by some mechanism of heat transfer into the heating zone. In addition to thermal diffusion, other forms of microscopic transport, such as mass diffusion and viscous transport, occur in the reaction zone. For astrophysical thermonuclear combustion of degenerate material, thermal diffusion dominates all other forms of microscopic transport (see Timmes & Niemeyer 2000). Thus these other forms of transport are neglected here. The products of the reaction are assumed to be in a state of thermal equilibrium. The rate at which the fuel burns is controlled by the reaction rate. In this paper I use a simplified reaction-diffusion model. I assume a one-step Arrhenius kinetics with constant and anisotropic heat conduction coefficients. In addition I assume an ideal gas equation of state. The direction of propagation of flames is in the z direction in the $z - x$ plane. The simulations of flame propagation are 1.5-dimensional in the sense that vector quantities (i.e. the magnetic field and velocity) have both z and x components but their only spatial dependence is the z coordinate. The equations describing the conservation of mass, momenta,

and total energy densities in the flame in 1.5-dimensions (1.5D) are

$$\frac{\partial \rho}{\partial t} + \frac{\partial \rho u_z}{\partial z} = 0, \tag{2.1}$$

$$\frac{\partial \rho u_z}{\partial t} + \frac{\partial}{\partial z}\left(\rho u_z^2 + P + \frac{H_x^2 - H_z^2}{8\pi}\right) = 0, \tag{2.2}$$

$$\frac{\partial \rho u_x}{\partial t} + \frac{\partial}{\partial z}\left(\rho u_x u_z - \frac{H_x H_z}{4\pi}\right) = 0, \tag{2.3}$$

$$\frac{\partial U}{\partial t} + \frac{\partial}{\partial z}\left(u_z\left(\frac{1}{2}\rho(u_z^2 + u_x^2) + \rho\epsilon + P\right) + \frac{H_x^2 u_z}{4\pi} - \frac{H_z H_x u_x}{4\pi} + q\right) = 0, \tag{2.4}$$

where ρ, $\mathbf{u} = (u_z, u_x)$, P, $\mathbf{H} = (H_z, H_x)$, U, ϵ, and q are the mass density, velocity vector, thermal pressure, magnetic field, total energy density $U = \rho(u_z^2 + u_x^2)/2 + \rho\epsilon + H^2/8\pi$, specific internal energy, and heat flux. The conservation equation for the x-component of the magnetic field is

$$\frac{\partial H_x}{\partial t} + \frac{\partial}{\partial z}\left(H_x u_z - H_z u_x\right) = 0. \tag{2.5}$$

The equation for the z-component of the magnetic field is the divergenceless equation in one-dimension,

$$\frac{\partial H_z}{\partial z} = 0. \tag{2.6}$$

The heat flux is

$$q = -\varkappa \frac{\partial T}{\partial z} \tag{2.7}$$

where T is the temperature and $\varkappa$ is the anisotropic heat conductivity given by

$$\varkappa = \frac{\varkappa_\perp H_x^2 + \varkappa_\parallel H_z^2}{H^2}, \tag{2.8}$$

Heat is transported most rapidly in the direction of field lines and is transported most slowly perpendicular to field lines. The level of anisotropy is parameterized by $\alpha = \varkappa_{\perp}/\varkappa_{\parallel}$,

$$\varkappa_{\parallel} = 2.9 \times 10^{-3} exp\left(\frac{\gamma Q_A}{(\gamma-1)Q}\right), \tag{2.9}$$

where Q_A is the activation energy of the reaction and Q is the energy released in the reaction. I assume an ideal equation of state with a fixed energy release,

$$P = \rho T, \epsilon = \frac{1}{\gamma - 1} T + QY \tag{2.10}$$

The equation for the conservation of the chemical variable is

$$\frac{\partial \rho Y}{\partial t} + \frac{\partial}{\partial z}\left(\rho u_z Y\right) = \rho R, \tag{2.11}$$

The variable Y tracks the progress of the reaction. It equals 1 in the fuel and decreases monotonically to 0 in the products of burning. The reaction rate is

$$R = -Y^2 e^{-Q_A/T}, \tag{2.12}$$

which follows one-step Arrhenius kinetics. Equations 2.1-2.12 define the set of equations of reactive flow magneto-hydrodynamics (RFMHD) in 1.5D.

2.2 Numerical Methodology

I use a cell-based code that solves numerically in conservative form the equations of reactive flow magneto-hydrodynamics. All conserved quantities are placed at the cell centers and the corresponding numerical fluxes are calculated at the cell boundaries. The spatial reconstruction of the fluxes is performed with the third-order accurate WENO finite dif-

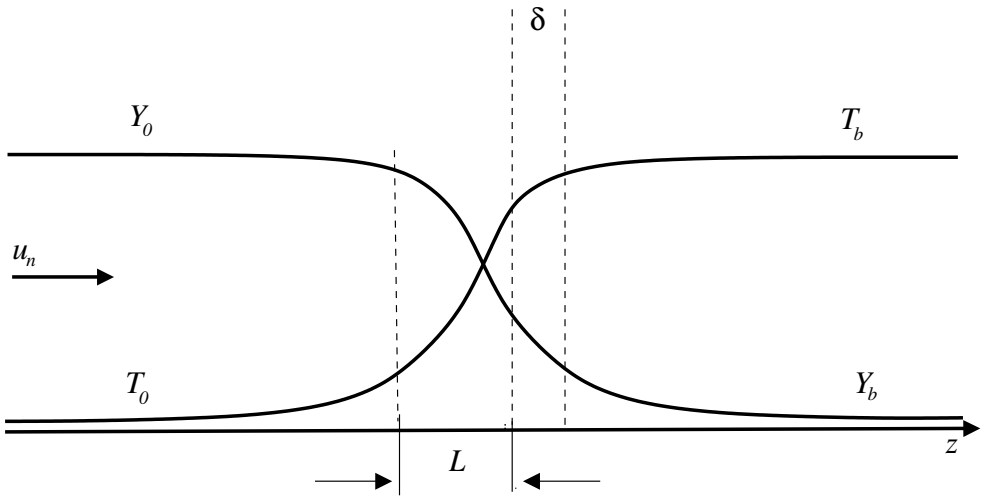

Figure 2.1: Simple sketch showing the composition and temperature distributions within a laminar flame. The region δ bounded by the two tall dashed lines is the reaction zone. The region L is the heating zone. The unburnt gas with initial composition Y_0 and temperature T_0 is located to the left of the heating zone. The products of burning with composition Y_b and temperature T_b are located to the right of the reaction zone. In the frame of reference of the flame, the unburnt gas moves towards the flame front at the speed u_n. This Figure is based on a similar figure that appears in Zeldovich et al. (1985).

ference algorithm, and temporal evolution is performed with the third-order accurate total variations-diminishing Runge-Kutta algorithm (Mignone et al. 2010). Thermal conduction is solved explicitly, and the fluxes of the conserved chemical quantity, ρY, are upwinded. Please refer to the Appendix to read about the performance of the code on a sample of MHD test problems that can be found in the literature.

I use the above described code to model the propagation of 1.5D, initially steady, laminar magnetized flames in different magnetized media. The calculation of steady-state flame solutions is carried out using the method described in RK16. I map these laminar flame solutions onto the computational grid and evolve them. To fit the flame to the computational grid, I extend the flame's tail to the right boundary. The boundary conditions are inflow/outflow along the direction of the flame normal.

CHAPTER 3

STEADY FLAME PROPERTIES AND CODE VERIFICATION

For the most part, the type of flame front simulated in this paper is a weakly magnetized super-Alfvénic laminar flame. As was shown in RK16, flames that originate from weakly magnetized media are super-Alfvénic. For the case of more strongly magnetized media, slow flames can develop as well.

Consider the propagation of a steady-state flame through a coherently magnetized medium (the following description of super-Alfvénic combustion is based on RK14). The direction of propagation of the flame front (i.e. the direction normal to the surface of the flame) is the z-direction, and the flame is in the $z - x$ plane. The angle of incidence between the flame front normal and the upstream magnetic field is $\psi > 0$ radians. Suppose that the flame is super-Alfvénic, so that the velocity of the fluid in the upstream (fuel) and downstream (ashes) is between the Alfvénic and fast magnetosonic velocities. Within the reaction zone, the reaction energy powers an electric current $\mathbf{j}$ that flows perpendicular to the front surface in the $x - y$ plane. The current bends the magnetic field in the reaction zone toward the flame normal, weakening the magnetic field in the downstream. Through the action of the Lorentz force $\mathbf{F} \sim \mathbf{j} \times \mathbf{H}$, the burning fluid's velocity becomes nonzero in the x direction and points antiparallel to H_x.

Additionally, there are slow flames. The speed of the fluid in a slow flame is less than the slow magnetosonic velocity with respect to the upstream and downstream fluids. As material is burned during slow combustion, an electric current is generated out of the plane of the flame front in the opposite direction to the current generated in super-Alfvénic flames. As a result, the magnetic field in the reaction zone strengthens, and the Lorentz force pushes the reacting fluid in the direction parallel to H_x.

The time evolution of a super-Alfvénic flame front with isotropic heat transfer, $\alpha = \varkappa_\perp/\varkappa_\parallel = 1.0$, is shown in Figure 3.1. In this Figure, the initial structure of flame is shown,

its structure at $t = t_{burn}$, and the difference between the two. The parameter $t_{burn} = \delta_l / S_l$ is the combustion timescale, where δ_l is the laminar flame thickness and S_l is the flame speed. The flame thickness is calculated as

$$\delta_l = \frac{T_2 - T_1}{\max(|\frac{dT}{dz}|)}. \tag{3.1}$$

The flame front was evolved with the HSCD code and was not subject to any perturbations. The units for the idealized flame presented in this paper are such that in the fuel $\rho = 1.0$ and $T = 1.0$. The strength of the magnetic field is parameterized by $\beta^{-1} = H^2/(8\pi P)$, where initially $P \sim 1.0$ across the flame and H is taken to be the upstream magnetic field strength. In Figure 3.1 the magnetic field strength in the upstream fluid is $\beta^{-1} = 10^{-6}$. The angle of the magnetic field with respect to the flame front normal in the fuel is $\psi = 1.0$ radians. The flame maintains its structure to a high level after one burning time. However the flame solution does develop small unsteady motions as time elapses. This unsteadiness is believed to be due to numerical diffusion which has the effect of artificially expanding the flame's reaction zone.

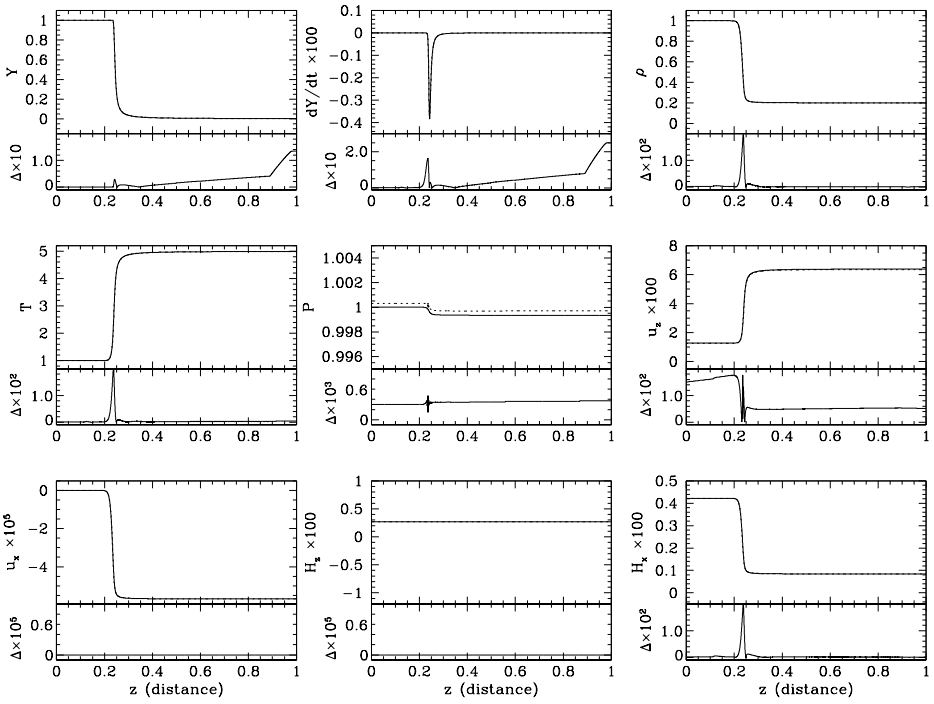

Figure 3.1: Time evolution of a steady laminar flame profile for super-Alfvénic combustion with $\alpha = \varkappa_\perp/\varkappa_\parallel = 1.0$. The initial upstream conditions are $\rho = 1.0$, $T = 1.0$, $Y = 1.0$, $u_z = 0.01280$, $\beta^{-1} = 10^{-6}$, and $\psi = 1.00$ radians. Each panel shows the variation of a certain physical quantity X at $t = 0.00$ (solid) and $t = t_{burn}$ (dotted), and the difference $\Delta = |X(t = t_{burn}) - X(t = 0.0)|/|X(t = 0.0)|$ between the two times.

CHAPTER 4

CONNECTION TO ASTROPHYSICAL FLAMES

Astrophysical thermonuclear combustion, as occurring in white dwarfs during Type Ia supernovae or on neutron stars during X-ray bursts, takes place in very dense and hot environments. For instance, during a Type Ia supernova densities can be as high as a few times 10^9 g cm^{-3}. During a neutron star X-ray superburst the density can be similarly high. Under such conditions, the electron component of the reacting plasma is degenerate and, especially for burning in the core of a white dwarf, is fully relativistic. The mode of heat transfer within the flame is some combination of electrons scattering off of ions, phonons, photons, and other electrons (see RK16 for a detailed description of the modes of heat conduction for the regime of relativistic degenerate thermonuclear combustion). Depending on the properties of the magnetized plasma, heat conduction will be anisotropic. The simulations presented here model anisotropic and isotropic heat conduction with constant conduction coefficients. Isotropic burning is motivated by degenerate thermonuclear flame propagation in magnetized environments where the largely isotropic electron-photon scattering conductivity dominates (e.g. for $10^6 < \rho < 10^8$ g cm^{-3} in Type Ia supernovae, see RK16). On the other hand, heat transported by way of electron scattering off of ions dominates the conductivity for high density degenerate plasma for densities $\rho > 10^8$ g cm^{-3}. This form of heat transport becomes highly anisotropic when there is a strong magnetic field present. I use constant anisotropic heat conductivity as a simple way of approximating the anisotropic transport of heat via electrons.

Unless stated otherwise, the starting ratio of magnetic to thermal pressure for the flames simulated in this paper is $\beta^{-1} = 10^{-6}$. For reference, a fluid composed of pure He with temperature $T = 10^8$ K and density $\rho = 10^6$ g cm^{-3} would have $\beta^{-1} = 10^{-6}$ if magnetized with a field of strength $H \sim 8.5{\times}10^8$ G. This type of fluid is characteristic of the burning layer on a neutron star during an X-ray burst. Meanwhile a fluid composed of 0.5 ^{12}C+0.5 ^{16}O

by mass with temperature $T = 10^8$ K and density $\rho = 10^7$ g cm^{-3} would have $\beta^{-1} = 10^{-6}$ if magnetized with a field of strength $H \sim 4.7 \times 10^9$ G. This higher density C+O fluid is more closely characteristic of the conditions in the intermediate layers of a white dwarf during a supernova. The flames then propagate up a magnetic field gradient. The final value of β^{-1} of the fluid after passing through the magnetic field gradient is $\beta^{-1} \sim 0.01$. For this value of β^{-1}, the same He fluid as before would be magnetized by a field of strength $H \sim 8.5 \times 10^{10}$ G. While the 0.5 ^{12}C+0.5 ^{16}O fluid would be magnetized by a field with strength $H \sim 4.7 \times 10^{11}$ G.

CHAPTER 5

RESULTS

I analyze the set of simulations of initially steady magnetized flames traveling through a medium with an inhomogeneous magnetic field. The magnetic field gradually increases from its initial value until reaching a maximum value at $t = t_{burn}/4$. During the period of magnetic field growth, the magnetic field is increased by $\Delta H \sim 1 \times 10^{-6}$ at the end of each time step. The code then runs without further external perturbations until $t = t_{burn}$. I will describe how the internal structure of initially steady super-Alfvénic flames changes after passing into the more strongly magnetized medium. Table 5.1 lists, for each simulation, the fuel's initial magnetic field orientation ψ, the initial field's strength β^{-1}, and the thermal conduction anisotropy parameter α. Two simulations with $\psi = 0$ radians (Table 5.1) were run to test the case when the magnetic field is aligned with the direction of flame propagation. As expected, during these simulations, the increasing strength magnetic field had no, or at most a negligible, effect on the thermal and kinematic properties of the simulated flames. The properties of a flame are disrupted only when the increasing strength magnetic field is at an angle $\psi > 0$ radians with respect to the direction of the flame. At the end of this Chapter, I will briefly examine the case of an initially steady strongly magnetized flame that travels through a decreasing strength magnetic field.

5.1 Internal flame structure

Figure 5.1 shows the transverse components of the magnetic field and velocity vector across two different super-Alfvénic flame fronts at various times after the flames move through the non-uniform magnetic field. The solid lines show the data for a flame with the isotropic thermal conduction and the non-solid lines show the data for the flame with the anisotropic conduction. For comparison, Figure 5.2 shows the u_x and H_x for two other flame simulations.

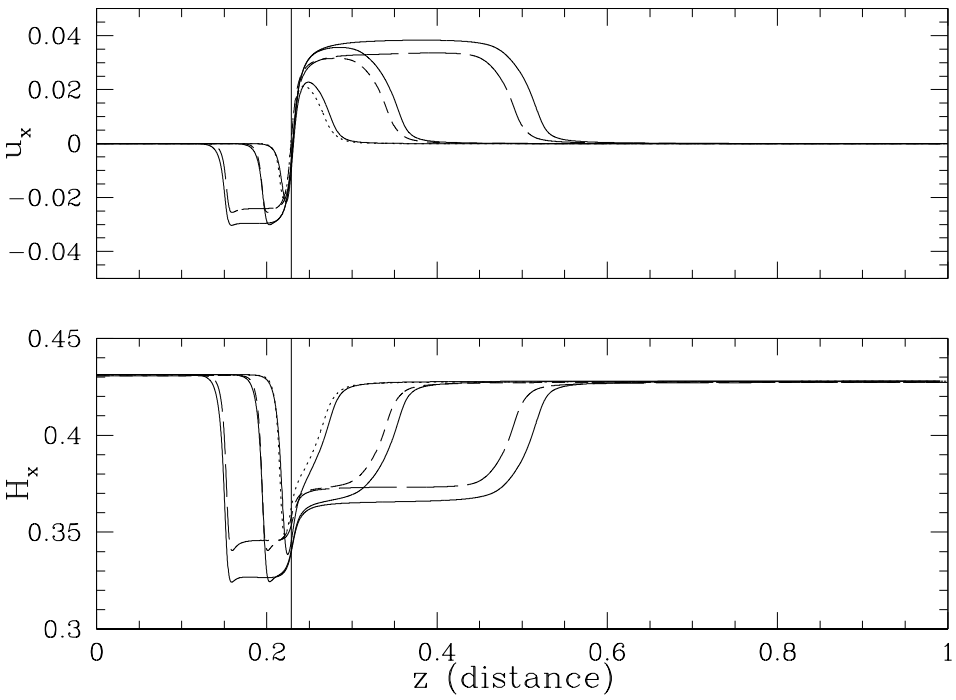

Figure 5.1: Snapshots of the H_x and u_x profiles of two different super-Alfvénic flames propagating into the more strongly magnetized medium. The non-solid curves show the data for the flame with initially $\beta^{-1} = 10^{-6}$, $\psi = 1.00$ radians, and $\alpha = 0.5$. Dotted curves – the profile at $t = t_{burn}/4$. Short dashed lines – the profile at $t = t_{burn}/2$. Long dashed lines – the profile at $t = t_{burn}$. For each non-solid line, the solid curve that closely follows it corresponds to the flame with the same initial field but with isotropic conduction ($\alpha = 1.0$) at the same time as the non-solid line. For reference, the vertical line denotes the approximate location of the initial center of the two flames where $Y \sim 0.5$.

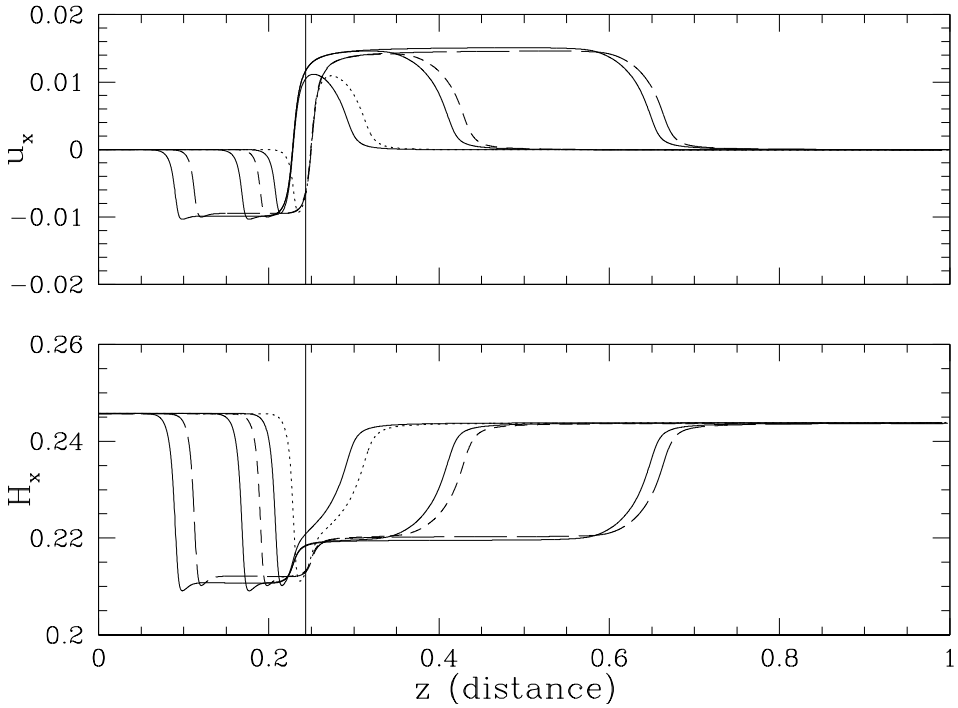

Figure 5.2: Same as Figure 5.1 but now the non-solid curves show the data for the flame with initially $\beta^{-1} = 10^{-6}$, $\psi = 0.5$ radians, and $\alpha = 0.5$. The solid curves are the data for the flame with the same initial field but with isotropic conduction ($\alpha = 1.0$) at the same time as the corresponding non-solid lines.

Table 5.1: The setups for the simulations

ψ (radians)	$\beta^{-1} = H^2/8\pi P$	$\alpha = \varkappa_\perp/\varkappa_\parallel$
0.0	10^{-6}	0.5
		1.0
0.5	10^{-6}	0.5
		1.0
1.0	10^{-6}	0.01
		0.1
		0.5
		1.0
1.25	10^{-6}	0.5
1.5	10^{-7}	0.5
	10^{-6}	0.5
		1.0
	10^{-5}	0.5
$\pi/2$	10^{-6}	0.5
		1.0

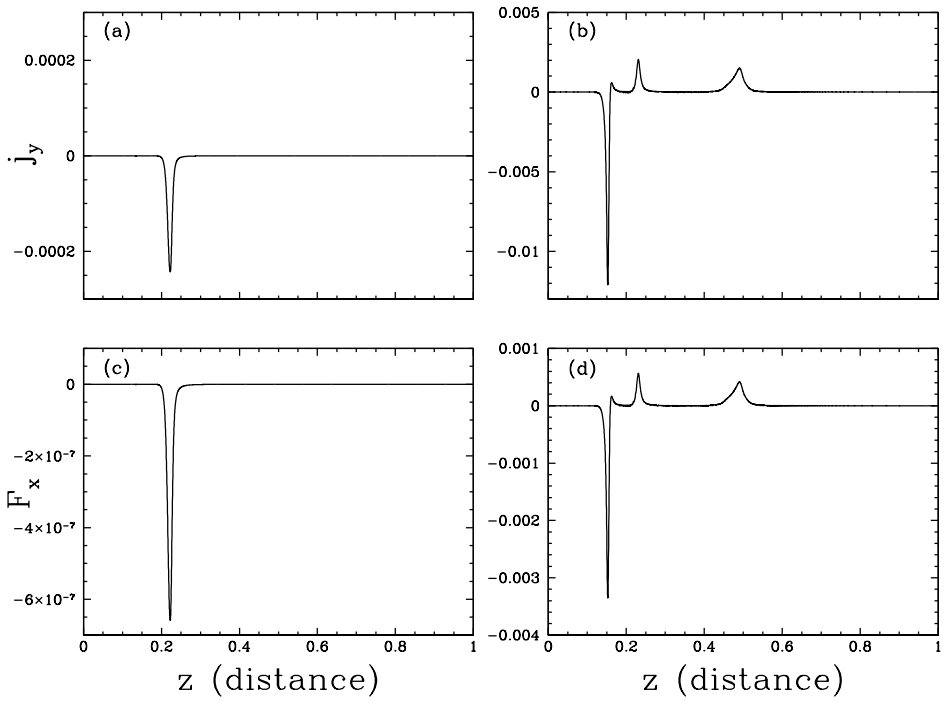

Figure 5.3: The current density j_y flowing out of the $z - x$ plane of the reaction front and the resulting Lorentz force F_x at $t = 0$ (panels (a) and (c)) and at $t = t_{burn}$ (panels (b) and (d)) for a super-Alfvénic flame with $\beta^{-1} = 10^{-6}$, $\psi = 1.00$ radians, and $\alpha = 0.5$.

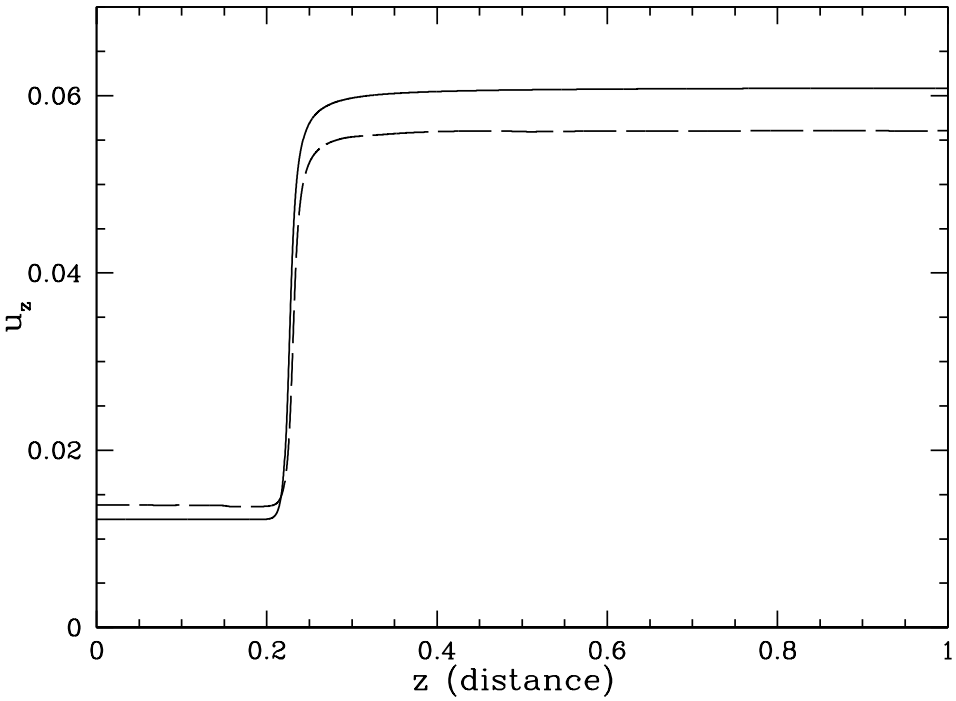

Figure 5.4: The u_z profile at $t = 0$ (solid) and $t = t_{burn}$ (dashed) for a super-Alfvénic flame with $\beta^{-1} = 10^{-6}$, $\psi = 1.00$ radians, and $\alpha = 0.5$.

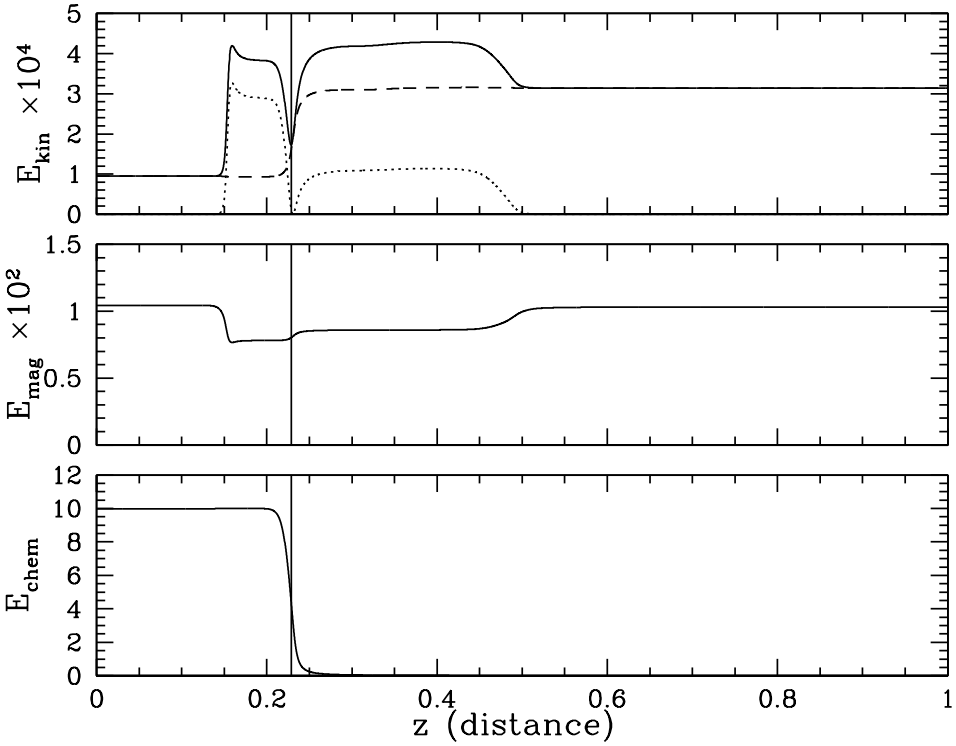

Figure 5.5: Components of the total energy density at $t = t_{burn}$ for a super-Alfvénic flame with $\beta^{-1} = 10^{-6}$, $\psi = 1.00$ radians, and $\alpha = 0.5$. In the top panel, the dashed curve represents $E_{kin,z} = (1/2)\rho u_z^2$, the dotted curve $E_{kin,x} = (1/2)\rho u_x^2$, and the solid curve $E_{kin} = E_{kin,z} + E_{kin,x}$.

The reaction of the flame to the new field is qualitatively similar, but differs in magnitude, for the flames in Figures 5.1 and 5.2. Instead of a monotonic decrease in the strength of the field across the flame front, the transverse magnetic field reaches a minimum in the fuel/reaction zone and then increases across the ashes and then becomes stationary. Recall that in a slow flame the transverse magnetic field increases across the reaction front. One can interpret the modified structure as being a hybrid of super-Alfvénic and slow flame profiles. The structure of the flame adjusts to the new stronger magnetic field and develops a magnetic field profile similar to a slow flame. The transverse velocity component behaves similarly and develops a strong shear across the flame. The transverse velocity component first decreases, which is characteristic of a super-Alfvénic flame, passes through a minimum and increases in the reaction zone before decreasing to its final value in the ashes. The increase in velocity in the reaction zone is characteristic of a slow flame.

While traveling through the inhomogeneous magnetic field, the flame reacts by developing a strong shear flow. The u_x shear is generated by an electric current j_y that propagates out of the plane of the front. Figure 5.3(a)-(b) show the initial and final j_y profiles for the anisotropic flame shown in Figure 5.1. The isotropic flame behaves similarly. The peaks in the current density at $t = t_{burn}$ are about one order of magnitude or more larger than the flame's initial current. Also, the peaks in the current density are coincident with the changes in the transverse component of the magnetic field (see Figure 5.1). It is the electric current density that is responsible for bending the field. The Lorentz force $F_x \sim j_y \times H_z$ is shown in Figure 5.3(c)-(d). The force, which grows by orders of magnitude during the simulation, pushes on the burning plasma, giving rise to the dramatic shear in the u_x profile.

RK14 found that even for a steady-state magnetized flame there is an induced electric current that flows in the $x - y$ plane. The energy responsible for this current is the reaction energy. The current results in Ohmic dissipation due to the plasma's finite electric conductivity. RK14 calculated that the total Ohmic dissipation rate inside the flame, $\dot{E}_{ohm}$, is

negligible compared to the integrated rate of burning, $\dot{E}_r$, in a thermonuclear flame. As a result, the energy allotted to the Ohmic dissipation is not significant in the overall energy budget of the flame. I show here that the induced electric current is 1 to 2 orders of magnitude larger for flames passing through increasing strength magnetic fields compared to passing through a uniform field. Consequently, there is a much larger rate of Ohmic dissipation expected. For instance, using the same numbers as in RK14 for a 0.5^{12}C+0.5^{16}O mixture, a current that is 100 times larger than the steady case would produce a ratio $\dot{E}_{ohm}/\dot{E}_r$ that is $\dot{E}_{ohm}/\dot{E}_r \simeq 10^{-5} - 10^{-3}$ for $\rho_1 = 10^7 - 10^9$ g cm^{-3}, respectively. The energy spent on Ohmic dissipation is still much smaller than the reaction energy. Furthermore, the energy responsible for the electric current largely comes from the non-uniform magnetic field energy and not the reaction energy.

The effect of the inhomogeneous magnetic field is to alter significantly the transverse velocity profile. For comparison, Figure 5.4 shows the evolution of the parallel component of the velocity for the anisotropic flame shown in Figure 5.1. The u_z profile shifts only slightly during the simulation, and the shift is even smaller for flames with isotropic heat conduction. At $t = t_{burn}$ the incoming u_z velocity has increased by a factor of ~ 1.12 over the initial incoming velocity and the outgoing velocity is ~ 0.93 lower. Other flame properties, like the density and temperature profiles and the reaction rate, are not modified by the changing magnetic field.

Figures 5.1 and 5.2 demonstrate that the result of introducing the strongly non-uniform field is in part the generation of the dramatic u_x shear. How does the energy locked into the shear flow compare to other forms of energy in the flame? Figure 5.5 shows various forms of energy at $t = t_{burn}$ for the anisotropic flame shown in Figure 5.1. Initially, the kinetic energy of the flame is due almost entirely to the plasma moving in the direction of the flame. This is the case despite the initial u_x shear in the unperturbed flame structure. As the simulation progresses the shear flow grows. By one burning time, the part of the

kinetic energy from the u_x velocity has grown to the magnitude of the z component. The magnetic energy also grows during the simulations as expected. The magnetic and kinetic energies, however, do not increase to the level of the chemical energy of the reaction front. The reaction front's chemical energy remains the dominant form of energy in the heating and reaction zones throughout the simulation.

5.2 Flame acceleration

As was referenced above in Figure 5.4, the speed of certain types of super-Alfvénic flames increases as they propagate up the magnetic field gradient. Here, the flame speed S is defined to be the value of u_z at $z = z_{fuel}$, where z_{fuel} is the position at which $T(z = z_{fuel}) - T(z = 0) > 0.01 \times \Delta z$. The amount a flame accelerates depends on the properties of the flame. The flame speed as a function of time is shown in Figure 5.6 for various super-Alfvénic flame solutions. The anisotropic flames with $\psi > 0$ (left panel of Figure 5.6) tend to accelerate to a peak velocity and then level off and eventually slow down once the magnetic field becomes constant. How much the flame accelerates depends sensitively on the initial field alignment. Additionally, as the initial field direction increases toward $\pi/2$, the initial flame speed decreases (see RK16). Conversely, flames that conduct heat isotropically (right panel of Figure 5.6) experience, independent of ψ, negligible levels of acceleration. Figure 5.7 shows flame speed at $t = t_{burn}$ as function of ψ. Only for large values of $\psi \lesssim \pi/2$ does the flame tend to accelerate to velocities of $\gtrsim 1.10$ times the initial flame speed. For $\psi \sim \pi/2$, the final flame speed does not differ much from the initial speed. The lack of large flame acceleration for the $\psi \sim \pi/2$ simulations may be due to strong heat transport suppression at large angles. The velocity of the flame at $t = t_{burn}$ is shown in Figure 5.7 not to be very sensitive to how strongly the flame is initially magnetized. Flames with $\beta^{-1} = 10^{-7}$, 10^{-6}, and 10^{-5} have approximately the same flame speed at $t = t_{burn}$ after propagating through the same inhomogeneous field.

Figures 5.6 and 5.7 show that the amount the flame accelerates is in part dependent on the degree of thermal anisotropy. To understand why this is the case, I refer to the conservation equation for the parallel component of the momentum (Equation 2.2). Recall the u_z-profile at $t = t_{burn}$ for an accelerating flame shown in Figure 5.4. This representative example shows that the upstream plasma velocity increased relative to the initial upstream velocity by $t = t_{burn}$, and in the downstream the velocity decreased relative to the initial profile. In the fuel (upstream), the plasma density remains nearly constant and uniform as the flame propagates through the inhomogeneous magnetic medium. The density also remains nearly constant and uniform in the ashes (downstream). Therefore, for the fuel and ashes, I can simplify Equation 2.2 to obtain an approximate equation for the parallel component of the plasma velocity. That is, for the region of the flame where the fuel resides

$$\frac{\partial u_{z,fuel}}{\partial t} + \frac{\partial}{\partial z}\left(u_{z,fuel}^2 + P_{fuel}/\rho_{fuel} + \frac{H_{x,fuel}^2 - H_{z,fuel}^2}{8\pi\rho_{fuel}}\right) = 0, \tag{5.1}$$

and for the region of the flame where the ashes are

$$\frac{\partial u_{z,ash}}{\partial t} + \frac{\partial}{\partial z}\left(u_{z,ash}^2 + P_{ash}/\rho_{ash} + \frac{H_{x,ash}^2 - H_{z,ash}^2}{8\pi\rho_{ash}}\right) = 0, \tag{5.2}$$

where ρ_{fuel} and ρ_{ash} are approximately constant and uniform. Also note that across the flame the parallel component of the magnetic field, H_z, does not change (Equation 2.6). Therefore, changes in the velocity of plasma fuel and ash can be explained by gradients in u_z^2, gradients in the thermal pressure P, and gradients in the magnetic pressure $H_x^2/8\pi$. As described above, the inhomogeneous magnetic field induces large gradients in the H_x profile (see Figures 5.1 and 5.2). In the fuel, there is a large negative H_x gradient and, therefore, a large negative gradient in the magnetic pressure. To measure the magnitude of the decrease in the fuel's magnetic pressure, I make use of the following definitions. I define z_{MP1} to be the position in the fuel where the magnetic pressure, modulo $1/8\pi$, begins to decrease

$H_x^2(z = z_{MP1}) - H_x^2(z = z_{MP1} - \Delta z) > 0.1 \times \Delta z$. I define z_{MP2} to be the position in the fuel where the magnetic pressure is at a minimum. The measure of the fuel's magnetic pressure gradient is then $GRAD(H_x^2) = |H_x^2(z = z_{MP2}) - H_x^2(z = z_{MP1})|/(z_{MP2} - z_{MP1})$. I plot the speed up factor of the flame's fuel at $t = t_{burn}$ and $GRAD(H_x^2)$ as functions of the thermal anisotropy parameter α in Figure 5.8. First, the magnitude of the change in the fuel's magnetic pressure is positively correlated with the flame's acceleration. The sharper the decrease in the upstream magnetic pressure, the more the flame accelerates. This can be explained by the fact that the magnetic pressure gradient exerts a force on the plasma that accelerates the fuel. The second observation to be made from Figure 5.8 is that the magnitude of the upstream magnetic pressure gradient is larger for more thermally anisotropic conditions (i.e. smaller α). To account for the decrease in the plasma speed relative to the initial speed in the ashes (see, again, Figure 5.4), I note that the decrease in the magnetic pressure in the fuel is followed by a steady increase in the magnetic pressure. The magnetic pressure increases until it reaches an equilibrium value (see, again, Figures 5.1 and 5.2). Therefore, the burning plasma in the heating and reaction zones of the flame is slowed by an increasing magnetic pressure.

The resolution of the simulation may play a role in influencing the properties of the flame as it evolves. To test this possibility, I simulated the evolution of super-Alfvénic flames at different grid resolutions (Figure 5.9). Figure 5.7 shows that the speed of flames at $t = t_{burn}$ relative to the initial speed. The data in Figure 5.7 are from simulations with $N = 2^{12} = 4096$ cells across the grid from $z = 0$ to $z = 1$. Figure 5.9 reveals that the flame speed at $t = t_{burn}$ tends to increase with increasing resolution. This suggests that the influence of the inhomogeneous magnetic medium is indeed to accelerate the flame. Hence, the data presented in Figure 5.7 can be interpreted as lower limits on the flame speed.

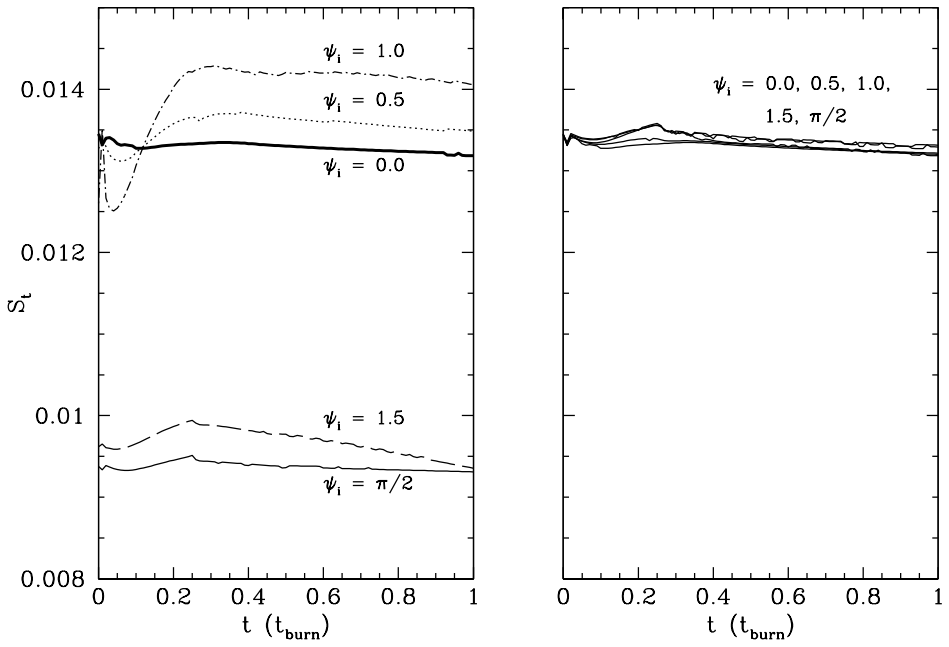

Figure 5.6: Flame speed S as a function of time for various super-Alfvénic flames with $\beta^{-1} = 10^{-6}$ that move through an increasing strength magnetic field. Left panel – flame solutions with anisotropic heat conduction. Right panel – flame solutions with isotropic heat conduction. The units for the ψ labels are radians.

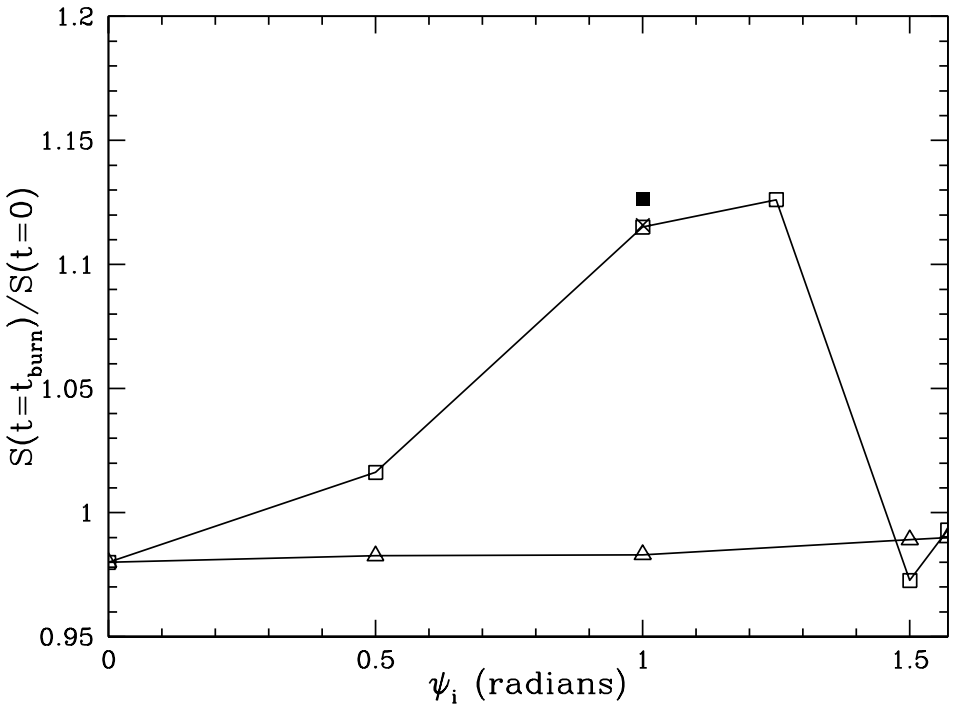

Figure 5.7: Ratio of the flame speed S at $t = t_{burn}$ to the flame speed at $t = 0$ as a function of the initial upstream magnetic field orientation ψ for various super-Alfvénic flame solutions. Open squares – anisotropic flames with $\beta^{-1} = 10^{-6}$ initially. Closed square – anisotropic flame with $\beta^{-1} = 10^{-5}$. Cross – anisotropic flame with $\beta^{-1} = 10^{-7}$. Triangles – isotropic flames with $\beta^{-1} = 10^{-6}$.

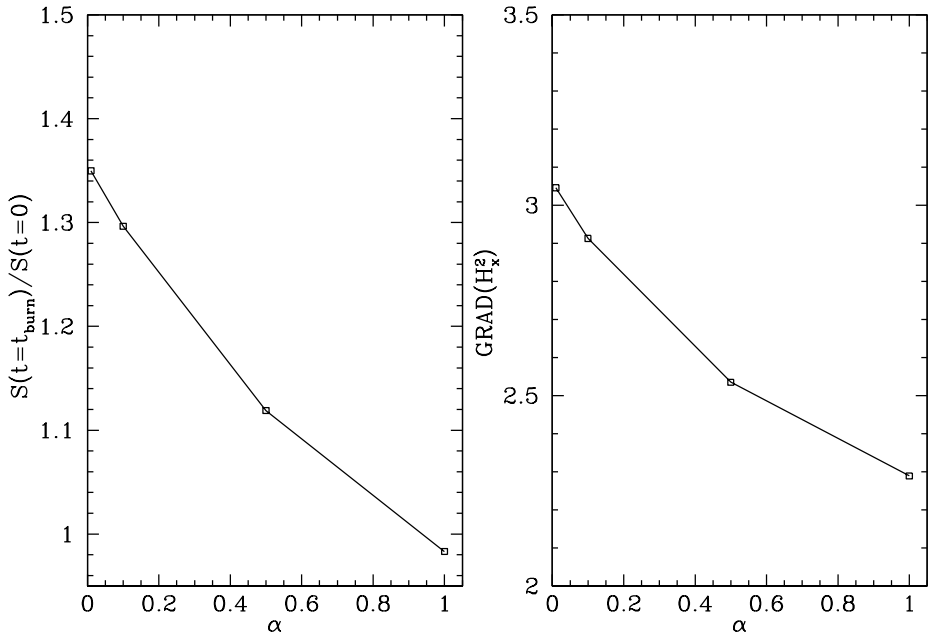

Figure 5.8: Super-Alfvénic flame data for flames with $\beta^{-1} = 10^{-6}$ and $\psi = 1.00$ radians after having propagated through the increasing strength magnetic field. Left panel – the ratio of the flame speed S at $t = t_{burn}$ to the flame speed at $t = 0$ as a function of the thermal anisotropy parameter α. Right panel – the quantity $GRAD(H_x^2)$ at $t = t_{burn}$ as a function of the thermal anisotropy parameter α. The quantity $GRAD(H_x^2)$ measures the magnitude of the decrease in the magnetic pressure in the fuel.

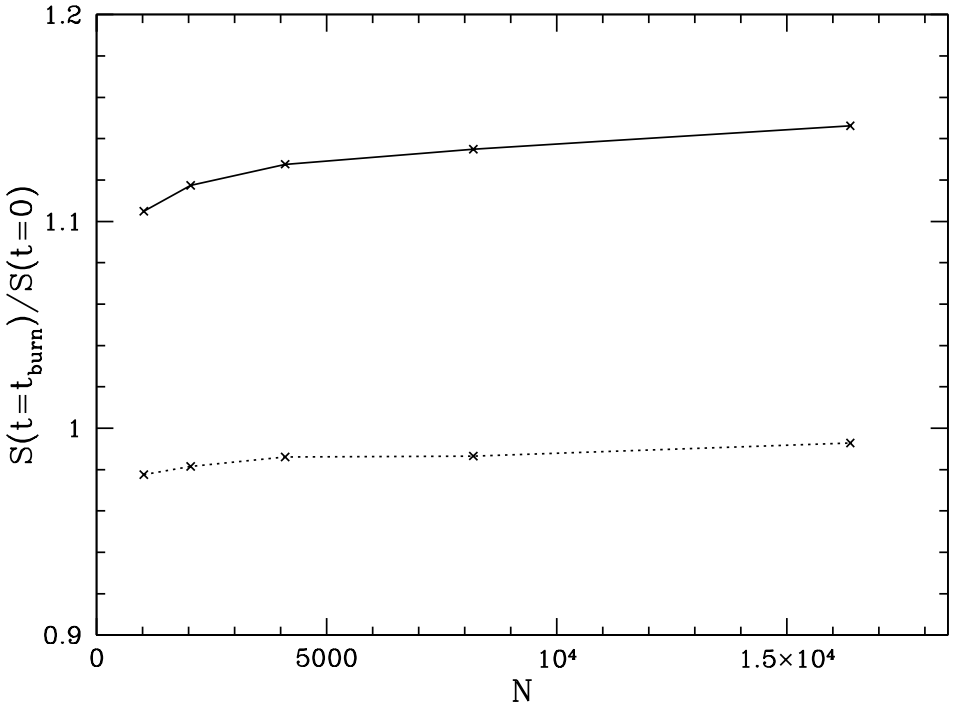

Figure 5.9: Ratio of the flame speed S at $t = t_{burn}$ to the flame speed at $t = 0$ as a function of the number of cells N in the simulation. The solid line connects the flame speed data for $\beta^{-1} = 10^{-6}$, $\psi = 1.00$ radians, and $\alpha = 0.5$. The dashed line connects data for $\beta^{-1} = 10^{-6}$, $\psi = 1.00$ radians, and $\alpha = 1.0$.

5.3 Flame propagation from a strongly to weakly magnetized medium

Whether a flame moves through a white dwarf interior during a supernova or over the surface of a neutron star during an X-ray burst, the medium through which the flame travels will likely possess a magnetic field that has been tangled as a result of pre-explosion turbulent mixing. To this point, I have considered the simplified simulation setup of a magnetized flame moving up a magnetic field gradient. I now consider a similar problem but where the environment's magnetic field decreases monotonically from an initially strong field to a weak one. For the simulation presented here, I map to the computational grid a steady slow combustion flame with $\psi = 1.00$ radians and $\alpha = 0.5$. During the simulation the flame moves down a magnetic field gradient. The initial ratio of magnetic to thermal pressure is $\beta^{-1} \sim 10^{-2}$ and the final value is $\beta^{-1} \sim 8 \times 10^{-6}$. I show in Figure 5.10 the simulated flame's H_x and u_x profiles as a function of time. Unlike for the increasing field strength simulations (see Figures 5.1 and 5.2), a strong shear flow is not generated. Without the shear flow in the upstream medium, a magnetic pressure gradient is not formed in the fuel. As a result, the flame does not accelerate. Previously, I described the modified structure of a super-Alfvenic flame, which has propagated up a magnetic field gradient, as being a hybrid of steady super-Alfvenic and slow flame profiles. In the case of a super-Alfvenic flame moving down a magnetic field gradient, the hybrid structure does not develop. One can interpret this result by using the fact that steady slow flame solutions only exist when the magnetic field is strong (see RK16), and, therefore, the super-Alfvenic flame that moves down a gradient does not take on the structural properties of a slow flame. Lastly, at the end of the simulation, the flame speed relative to its initial speed is ~ 0.89. The deceleration of the flame is consistent with the eventual gradual slowing of all the simulated flames in this paper (see Figure 5.6).

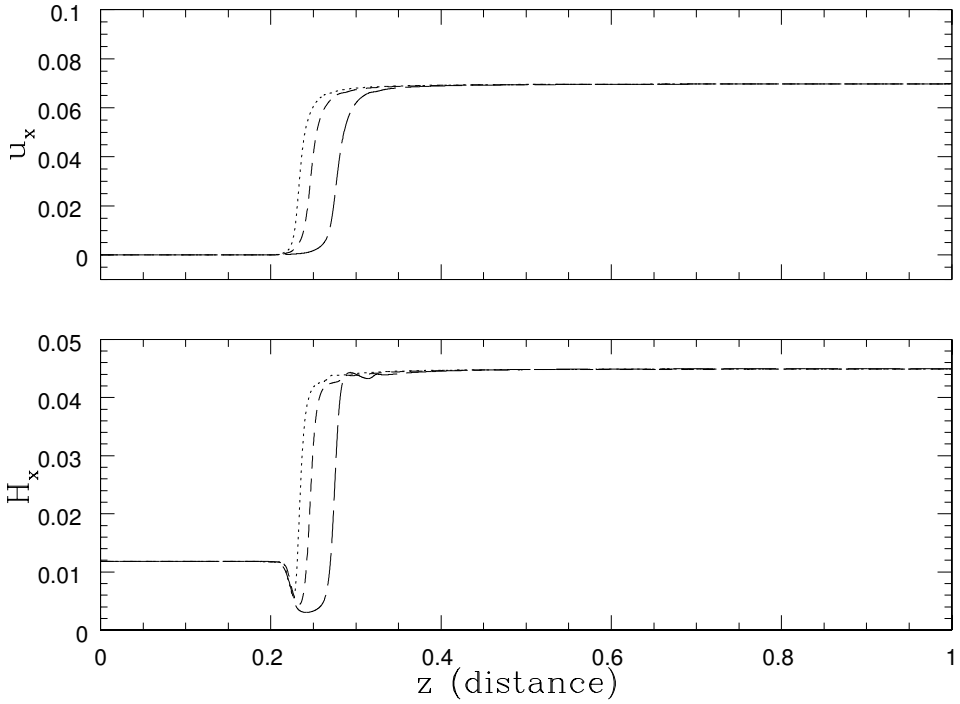

Figure 5.10: Snapshots of the H_x and u_x profiles of a slow combustion flame as it propagates through a decreasing strength magnetized medium. Initially, the properties of the flame are $\beta^{-1} = 10^{-2}$, $\psi = 1.00$ radians, and $\alpha = 0.5$. Dotted curves – the profile at $t = t_{burn}/4$. Short dashed lines – the profile at $t = t_{burn}/2$. Long dashed lines – the profile at $t = t_{burn}$.

CHAPTER 6

DISCUSSION AND CONCLUSIONS

This paper dealt with the physics of weakly magnetized super-Alfvénic flame propagation through non-uniform magnetic media. The solutions for the steady flames, which served as the initial conditions for the simulations, were obtained using the procedure in RK16. The non-steady properties of a flame traveling through a non-uniform field depend on certain conditions, such as the orientation of the flame relative to magnetic field and whether the flame conducts heat anisotropically or not. The decision to model idealized flames was made in order to study how inhomogeneities in a magnetic medium affect the basic properties of flames (i.e. speed and structure) and to avoid complicating the problem with, for instance, the nuclear kinetics of thermonuclear burning. Nevertheless, careful consideration must be applied when drawing conclusions about astrophysical flames based on the idealized simulations in this paper. The analysis in Chapter 5 provides important qualitative clues about the behavior of thermonuclear flames that may develop during SNe Ia or X-ray bursts to name two examples.

Flames that propagate up magnetic field gradients develop strong shear flows. The Lorentz force, $F_x \sim j_y \times H_z$, accelerates the plasma and generates the transverse shear. The direction of the Lorentz force is controlled in the flame by the direction of the electric current j_y. The magnetic energy introduced by the increasing strength magnetic field induces pulses of electric current that alternate in direction from the flame front into the products of burning. The alternating directionality of the current creates an alternating direction for the Lorentz force that ultimately forms the shear. The shear flow occurs for anisotropically and isotropically conducting flames. However, the magnitude of the shear is sensitive to the degree of thermal anisotropy with a larger shear for more anisotropic flames. The shear flow is expected to have a destabilizing effect on the flame. This destabilizing effect may accelerate the transition to turbulent burning. For Type Ia supernovae, a quicker transition

to turbulent burning would lead to quicker mixing of the burning layers in the white dwarf. To explore further the shear in the flame introduced by the inhomogeneous magnetic field and the resulting potential instability, a follow-up analysis of two- and three-dimensional simulations of magnetized flame propagation is called for. In any event, this paper shows that one effect of the inhomogeneous magnetic medium on the flame is to power alternating currents in the flame that power a shear flow in the plasma.

The inhomogeneous magnetic field was also shown to alter, for flames with certain properties, the flame speed. The flame speed in this paper was taken to be the value of u_z at $z = z_{fuel}$, where z_{fuel} is the position at which $T(z = z_{fuel}) - T(z = 0) > 0.01 \times \Delta z$. For anisotropic flames, the simulations presented revealed that flames that travel relative to the magnetic field at an angle $0 < \psi \lesssim \pi/2$ accelerate as they move up the magnetic field gradient. For example, after one burning time, the flame with $\psi = 1.0$ radians and $\alpha = 0.5$ had accelerated to 1.12 times its initial speed. On the other hand, the flame speed for isotropic flames changes negligibly when exposed to the non-uniform field. With increased resolution of the simulation, it was shown that the final flame speed also increases. It is therefore the case that the speed has not converged, but the direction of the change in the speed as a function of the simulation resolution suggests that the increasing strength magnetic field does accelerate the flame. Naturally occuring thermonuclear flames may accelerate under similar circumstances. For instance, as a flame during a SN Ia propagates through the white dwarf it may speed up as it encounters magnetic field inhomogeneities. The acceleration of the flame might then contribute to the suppression of flame front wrinkling, delaying the onset of turbulent combustion. However, this effect would potentially be in competition with the destabilizing effect of the shear flow mentioned in the previous paragraph. In the case of an X-ray burst, flame acceleration due to magnetic field inhomogeneities in the burning layers of the neutron star would speed up the consumption of the fuel and shorten the rise time of the observed burst's light curve. More realistic modeling of flame propagation during X-ray

bursts that include non-uniform magnetic fields would provide a more conclusive answer regarding the role of magnetic fields during X-ray bursts. However, this work provides evidence that in general a flame interacting with a non-uniform magnetic field, which conducts heat anisotropically, will tend to accelerate.

REFERENCES

Balsara, D.S. & Spicer, D.S., 1999, J. Comput. Phys., 149, 270.

Calleja, A. C., 2006, University of Chicago Ph.D. thesis.

Cavecchi, Y., Levin, Y., Watts, A. L., & Braithwaite, J., 2016, MNRAS, 459, 1259.

Cumming, A. & Bildsten, L., 2001, ApJ, 559, L127.

Dedner, A., Kemm, F., Kröner, D., Munz, C.-D., Schnitzer, T., Wesenberg, M., 2002, J. Comput. Phys., 175, 645

Fujimoto, M. Y., 1993, ApJ, 419, 768

Galloway, D. K., Muno, M. P., Hartman, J. M., Psaltis, D., & Chakrabarty, D, 2008, ApJS, 179, 360.

Gamezo, V., Khokhlov, A., Oran, E., Chtchelkanova, A., & Rosenberg, R., 2003, Science, 299, 77.

Hillebrandt, W. & Niemeyer, J. C., 2000, ARA&A, 38, 191.

Hristov, B., Collins, D. C., Hoeflich, P., Weatherford, C. A., & Diamond, T. R., 2018, ApJ, 858, 13

Keek, L., Langer, N., & in't Zand, J.J.M., 2009, A&A, 502, 871

Mignone, A., Bodo, G., Massaglia, S., Matsakos, T., Tesileanu, O., Zanni, C., Ferrari, A., 2007, ApJS, 170, 228

Mignone, A., Tzeferacos, P., & Bodo, G., 2010, J. Comput. Phys., 229, 5896

Piro, A. L. & Bildsten, L., 2007, ApJ, 663, 1252

Psaltis, D. & Chakrabarty, D., 1999, ApJ, 521, 332.

Reinecke, M., Hillebrandt, W., & Niemeyer, J. C.,2002, A&A 391, 1167

Remming, I. S. & Khokhlov, A. M., 2014, ApJ, 794, 87

Remming, I. S. & Khokhlov, A. M., 2016, ApJ, 831, 162

Ryu, D., & Jones, T.W., 1995, ApJ, 442, 228.

Timmes, F. X. & Niemeyer, J. C., 2000, ApJ, 537, 993.

Tóth, G., 2000, J. Comput. Phys., 161, 605.

Spruit, H.C., 2002, A&A, 381, 923.

Stone, J.M., Gardiner, T.A., Teuben, P., Hawley, J.F., Simon, J.B., ApJS, 178, 137

Watts, A. L. 2012, ARA&A, 50, 609.

Zeldovich, Ya. B., Barenblatt, G. I., Librovich, V. B., & Makhviladze, G. M., 1985, The Mathematical Theory of Combustion and Explosions (Plenum Publishing Corporation, New York)

Appendices

APPENDIX A

NUMERICAL TEST PROBLEMS

Here I describe the performance of HSCD on a suite of numerical MHD tests. The individual test problems were taken from various papers in the literature. Throughout this Appendix I compare the results of the code to popular astrophysical MHD codes. The codes I use for benchmarking are the Athena code (Stone et al. 2008) version 4.2 and the PLUTO code (Mignone et al. 2007) version 4.2. Athena can be downloaded at *https://princetonuniversity.github.io/Athena-Cversion/*, and PLUTO can be downloaded at *http://plutocode.ph.unito.it/*. For multi-dimensional MHD simulations, the HSCD code utilizes the generalized Lagrange multipler approach for the enforcement of the divergenceless condition on the magnetic field (Dedner et al. 2002; also see Mignone et al. 2010). The method couples to the conservative MHD equations an equation for the advection and diffusion of magnetic field divergence errors.

A.1 Circularly polarized Alfvén waves

For this problem, I use the setup from Mignone et al. (2010). I initialize on a periodic computational grid a circularly polarized Alfvén wave and follow its propagation. The amplitude

of the wave is set to $A = 0.2$. The initial values of the primitive variables are

$$\begin{Bmatrix} \rho \\ v_x \\ v_y \\ v_z \\ P \\ H_x \\ H_y \\ H_z \end{Bmatrix} = \begin{Bmatrix} 1.0 \\ 0.0 \\ Asin(\phi) \\ Acos(\phi) \\ 1.0 \\ \sqrt{4\pi} \\ A\sqrt{\rho}\sqrt{4\pi}sin(\phi) \\ A\sqrt{\rho}\sqrt{4\pi}cos(\phi) \end{Bmatrix} \tag{A.1}$$

The angle ϕ describes the rotation of the wave on the grid. In one dimension, the wave propagates along the grid axis ($\phi = 0$), where the grid extends from $x = \{0, 1\}$ and the wave has wavelength $\lambda = 1$. In two and three dimensions, the wave is rotated such that it is aligned with the grid's main diagonal. The specific values for ϕ for the different dimensions and the accompanying rotation matrix can be found in Mignone et al. (2010). After one period the L_∞ norm is calculated. The L_∞ norm for the vector of conserved variables at time t is defined to be

$$L_\infty = max|q^t - q^0|, \tag{A.2}$$

where q^0 is the vector of initial values of the conserved variables, and the maximum absolute difference is taken over the entire grid. In Figure A.1 I plot L_∞ for circularly polarized Alfvén waves after traveling a distance of one wavelength as a function of numerical resolution. The results show the convergence rate for the one-, two-, and three-dimensional versions of this test. The order of convergence of the errors is proportional to $\sim N^{-3}$ for the three dimensions.

To follow up on this test, I plot wave profiles for traveling and standing circularly polarized Alfvén waves after 5 wavelength crossing times for the two-dimensional case in Figure A.2

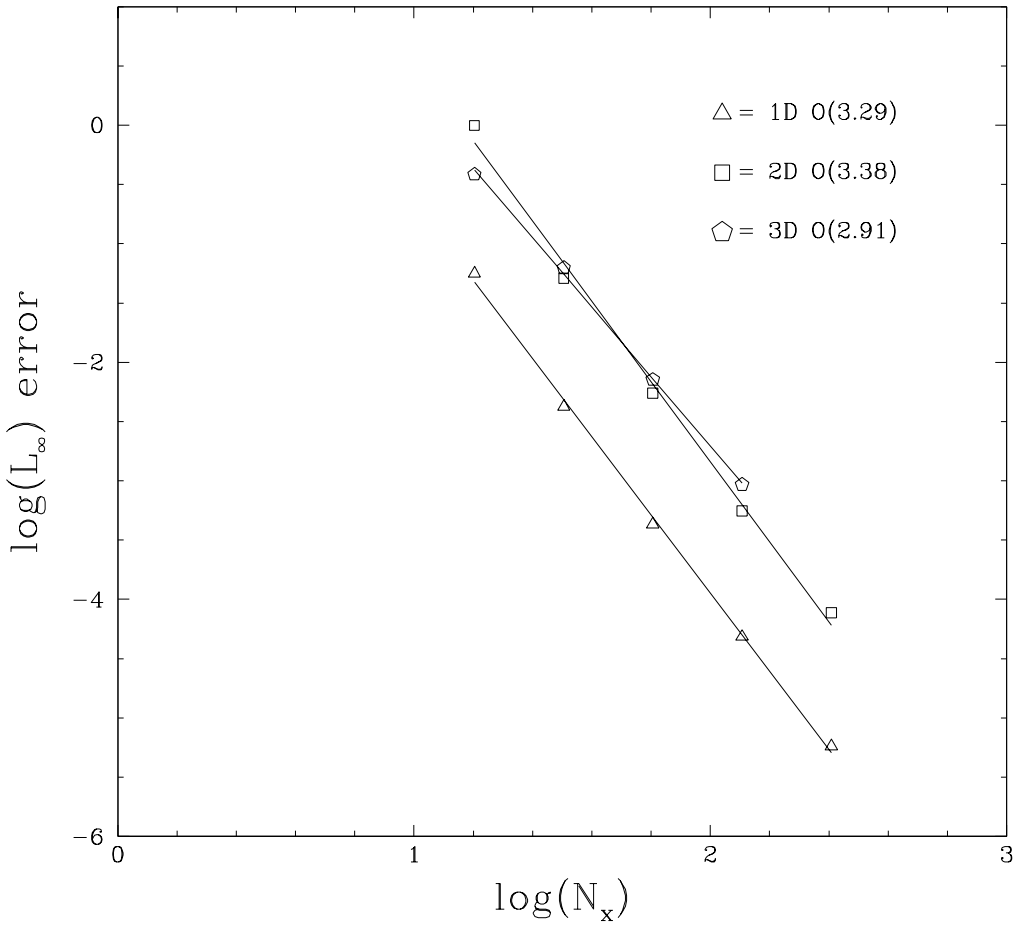

Figure A.1: Convergence of the norm of the L_∞ error for circularly polarized Alfvén waves after propagating a distance of one wavelength. Convergence for the one-dimensional (1D), 2D, and 3D versions of this problem are shown.

(c.f. Mignone et al. 2010). The Figure illustrates that at low resolution, traveling waves suffer from significant dissipation and dispersion.

A.2 shock tube problem

This version of the shock tube problem was originally presented in Ryu & Jones (1995). The initial discontinuity gives rise to discontinuities in each MHD wave family traveling in both the left and right directions. The initial left state of the fluid is $(\rho, v_x, v_y, v_z, p) = (1.08, 1.2, 0.01, 0.5, 0.95)$ with $(H_x, H_y, H_z) = (2, 3.6, 2)$. The initial right state is $(\rho, v_x, v_y, v_z, p) = (1.0, 0.0, 0.0, 0.0, 1.0)$ with $(H_x, H_y, H_z) = (2, 4, 2)$. In Figure A.3 I plot the results of the test using HSCD with $N = 512$ cells, and, for comparison, I plot the results of the test using the Athena code at the same resolution.

A.3 Magnetic rotor

This problem involves a central, rotating dense fluid with an initial magnetic field perpendicular to the disk's axis of rotation. For the setup of the problem I use the initial conditions described in Tóth (2000). Also see Balsara & Spicer (1999) for a detailed description of the motivation for this problem and the physics of it, which I will summarize below. For $r \leq r_0$ the density is $\rho = 10$, and the velocity components are $v_x = -v_0(y - 0.5)/r_0$ and $v_y = v_0(x - 0.5)/r_0$ where $v_0 = 2.0$. The parameter $r_0 = 0.1$ defines the central region of the disk. For $r_0 \leq r \leq r_1$ a linear taper in the density and the velocity separates the fast moving disk $r \leq r_0$ from the background state $r > r_1$. Within this taper region, $\rho = 1 + 9f$, and velocity components are $v_x = -fv_0(y - 0.5)/r$ and $v_y = fv_0(x - 0.5)/r$. The linear taper function is $f = (r_1 - r)/(r_1 - r_0)$. For $r > r_1$, the density is uniform $\rho = 1.0$ and the fluid is stationary. The background thermal pressure is $p = 1.0$ across the whole computational domain, while the background magnetic field is $(H_x, H_y, H_z) = (5, 0, 0)$. As the fluid

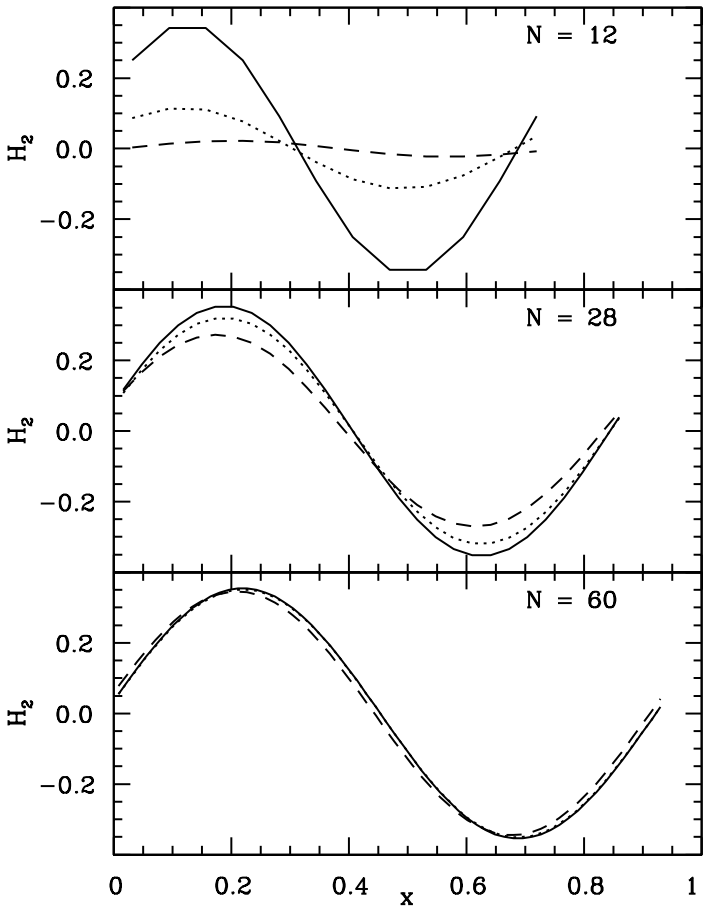

Figure A.2: The component of the magnetic field along the x_2-axis after 5 wavelength crossing times for circularly polarized Alfvén waves at $N = [12, 28, 60]$. The solid curve in each panel is the wave profile at $t = 0$, the dotted curve is the standing wave profile, and the dashed curve is the traveling wave profile.

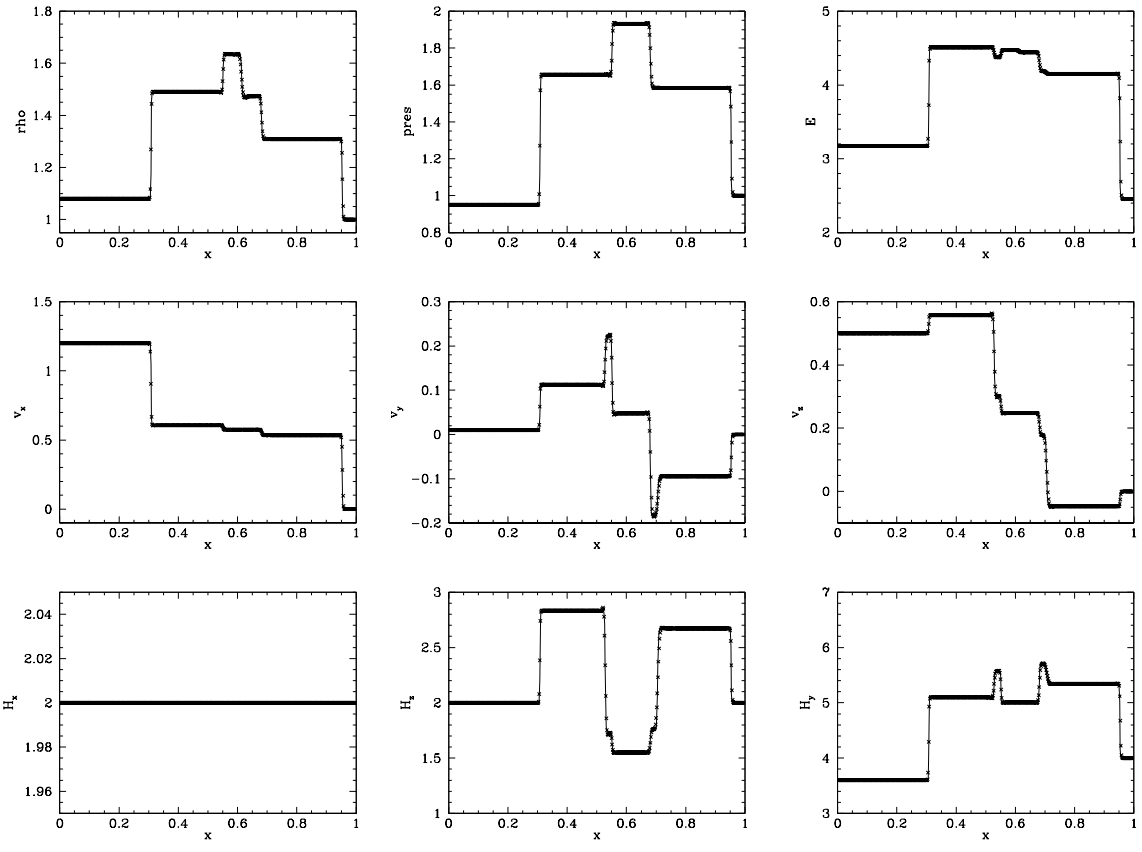

Figure A.3: Results from the Ryu & Jones (1995) 1D shock tube problem for 512 cells at $t = 0.2$. The squares represent HSCD data, while the solid curves represent data from the Athena code at the same resolution.

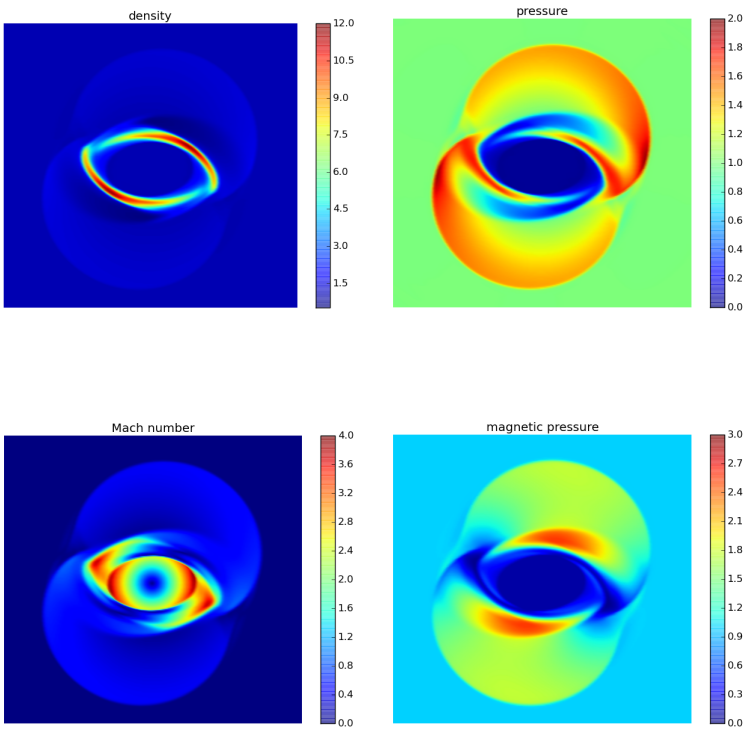

Figure A.4: Density, pressure, Mach number, and magnetic pressure at $t = 0.15$ for the MHD rotor problem at resolution N x $N = 256$ x 256 with HSCD data.

rotates field lines get distorted and torsional Alfvén waves are formed that propagate outward, releasing angular momentum. These losses in angular momentum slow down the disk. The disk expands as magnetic pressure builds up in the disk. This problem is motivated by angular momentum lose through Alfvén waves in star formation. The computational grid is square, and I chose the resolution N x $N = 256$ x 256. Figure A.4 shows surface plots of density, thermal pressure, thermal Mach number, and magnetic pressure at $t = 0.15$, which is before the boundaries take effect. These plots were inspired by similar plots that can be found in Stone et al. (2008). For comparison, the same surface plots for Athena and PLUTO are shown in Figures A.5 and A.6. In Figure A.7 I show in the top panel the H_y profile cut at $y = 0.5$ and in the bottom panel the H_x profile cut at $x = 0.5$. These cut plots were taken at the same time $t = 0.15$ as in Figures A.4-A.6.

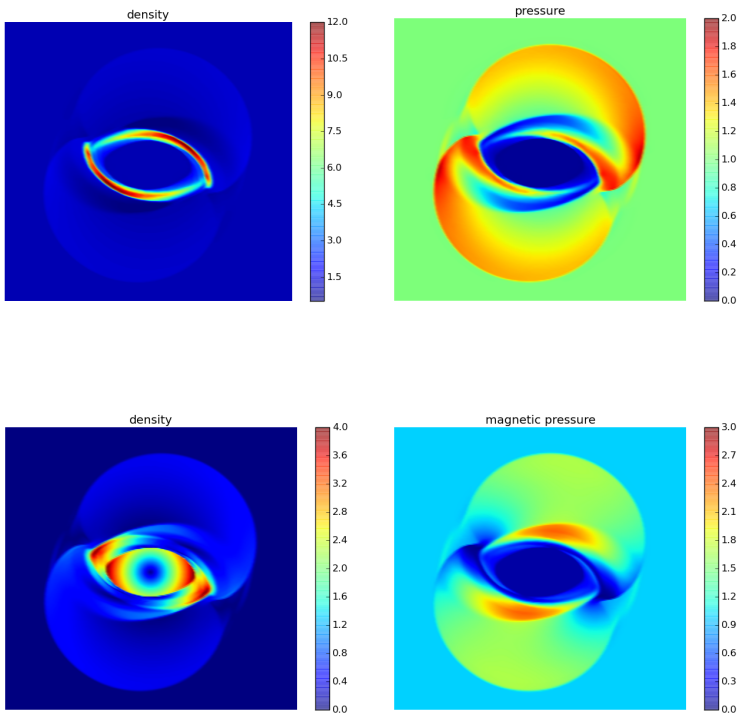

Figure A.5: Athena data for the MHD rotor problem at the same time and resolution as in Figure A.4.

A.4 Cloud-shock interaction

The setup for this problem can be found in Tóth (2000). This problem calculates the disruption of a high density cloud by a strong shock. The test is performed on a $N \times N$ grid with $x = \{0, 1\}$ and $y = \{0, 1\}$. There is a fixed boundary condition at $y = 1$ and the three other boundaries are zero-gradient. The initial discontinuity is located at $x = 0.6$. The left and right states are $(\rho, v_x, v_y, v_z, H_x, H_y, H_z)$ = (3.86859,0,0,0,167.345,0,2.1826182,-2.1826182) and (1, -11.2536,0,0,1,0,0.56418958,0.56418958). The high-density cloud is located at $x = 0.8$ and $y = 0.5$ with a radius 0.15, with density $\rho = 10$. The pressure P is 1 across the grid. Figures A.8 and A.9 show HSCD and PLUTO snapshots for this problem at $t = 0.06$, by which time the high density cloud has penetrated the shock layer. Cut plots are shown in Figure A.10.

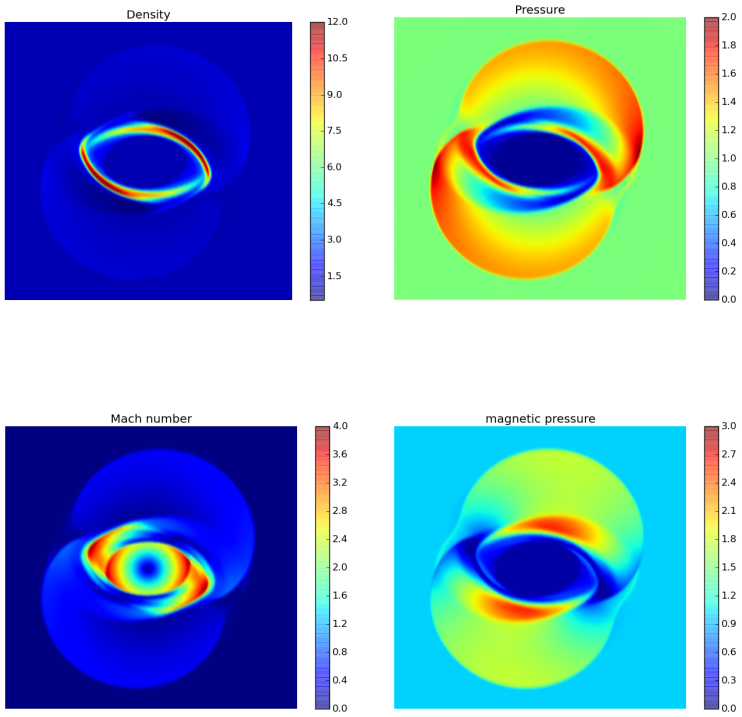

Figure A.6: PLUTO data for the MHD rotor problem at the same time and resolution as in Figure A.4.

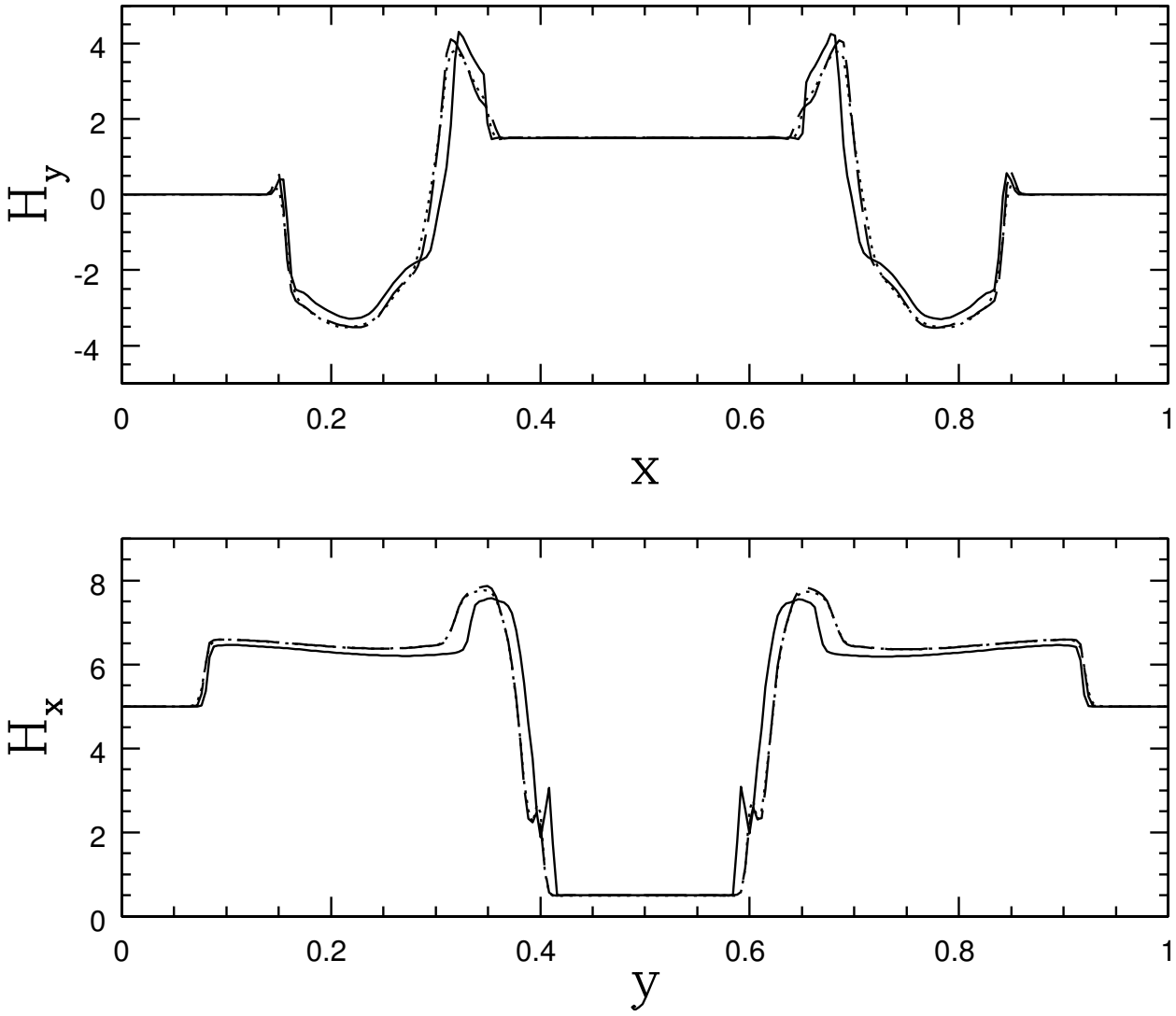

Figure A.7: Cut plots taken at $t = 0.15$ for the MHD rotor problem with HSCD (dotted), Athena (solid), and PLUTO (dashed). The profile of the y-component of the magnetic field at $y = 0.5$ is shown in the top panel, and the profile of the x-component of the magnetic field at $x = 0.5$ is shown in the bottom panel.

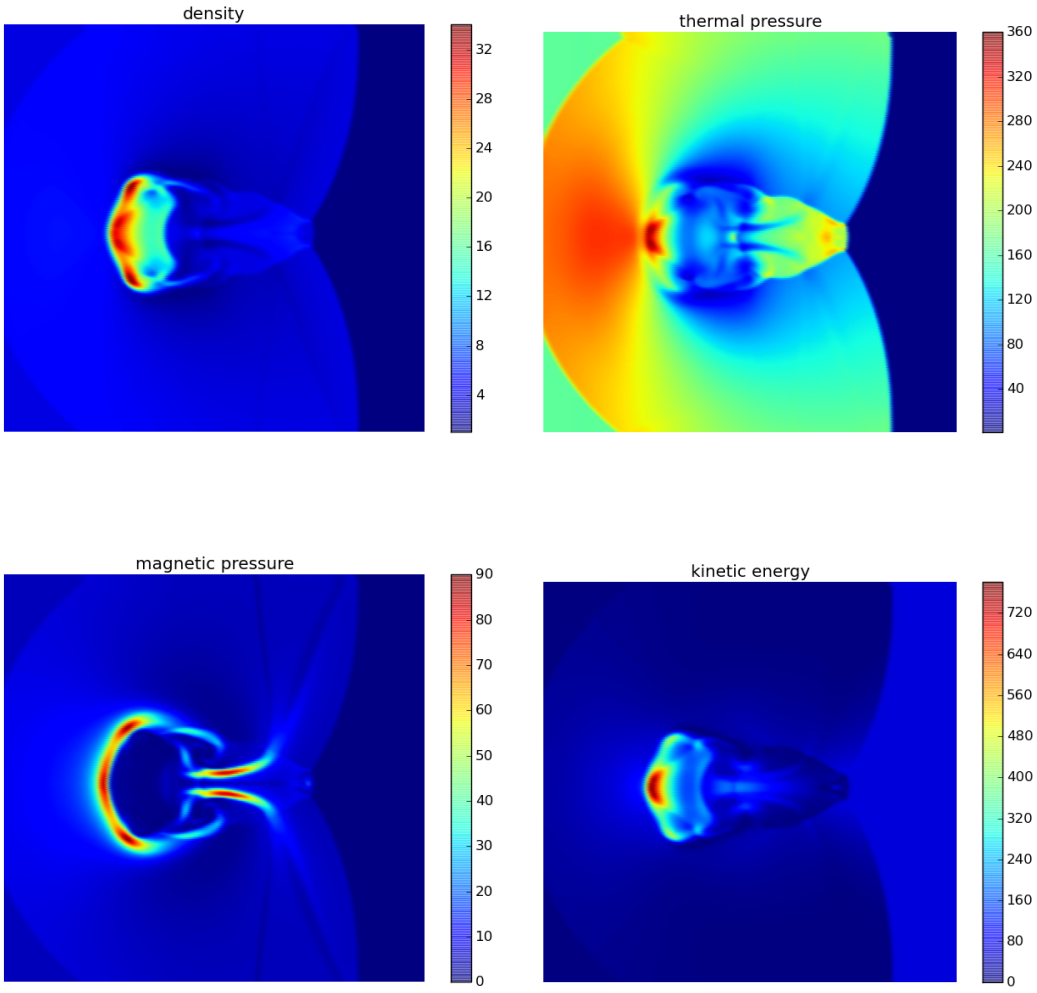

Figure A.8: Density, thermal pressure, magnetic pressure, and specific kinetic energy at $t = 0.06$ for the magnetized cloud-shock problem at resolution N x $N = 256$ x 256 with HSCD data.

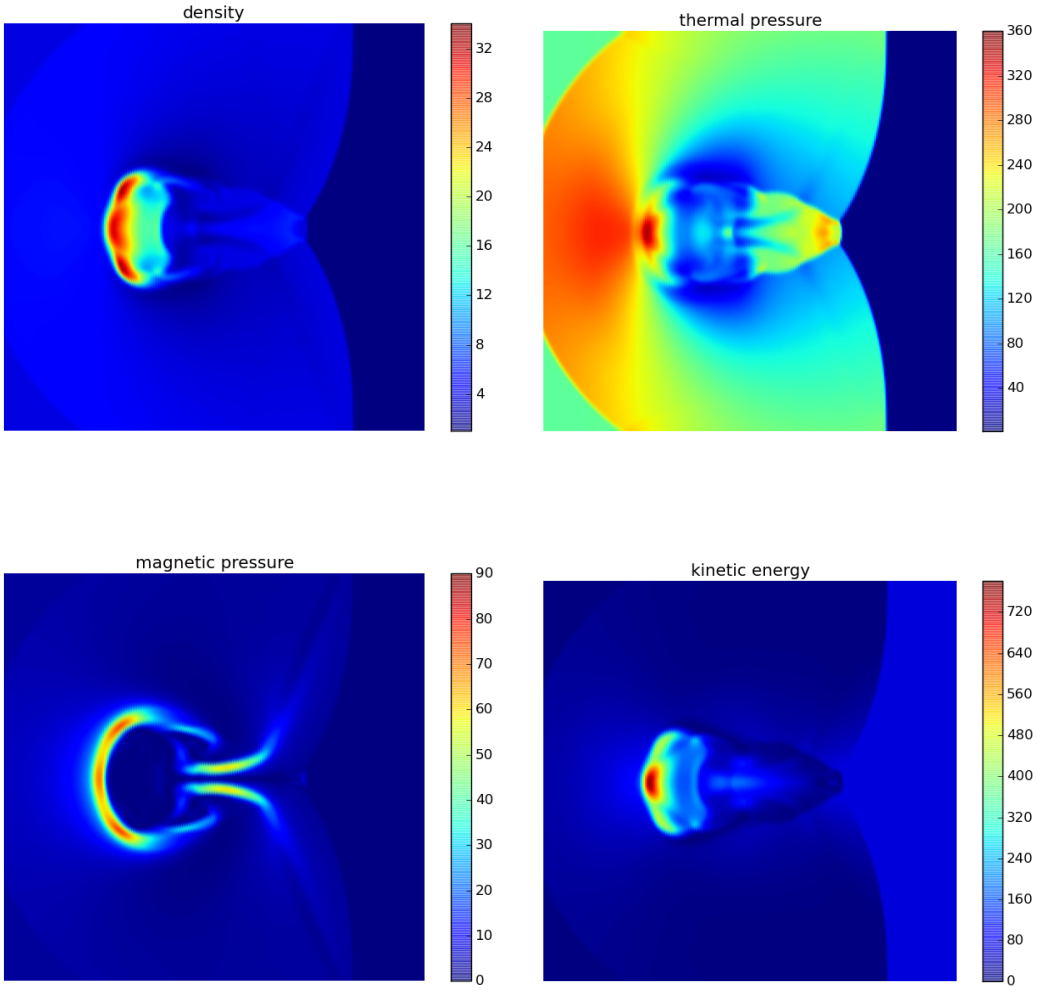

Figure A.9: The magnetized cloud-shock problem with PLUTO data at the same time and resolution as in Figure A.8.

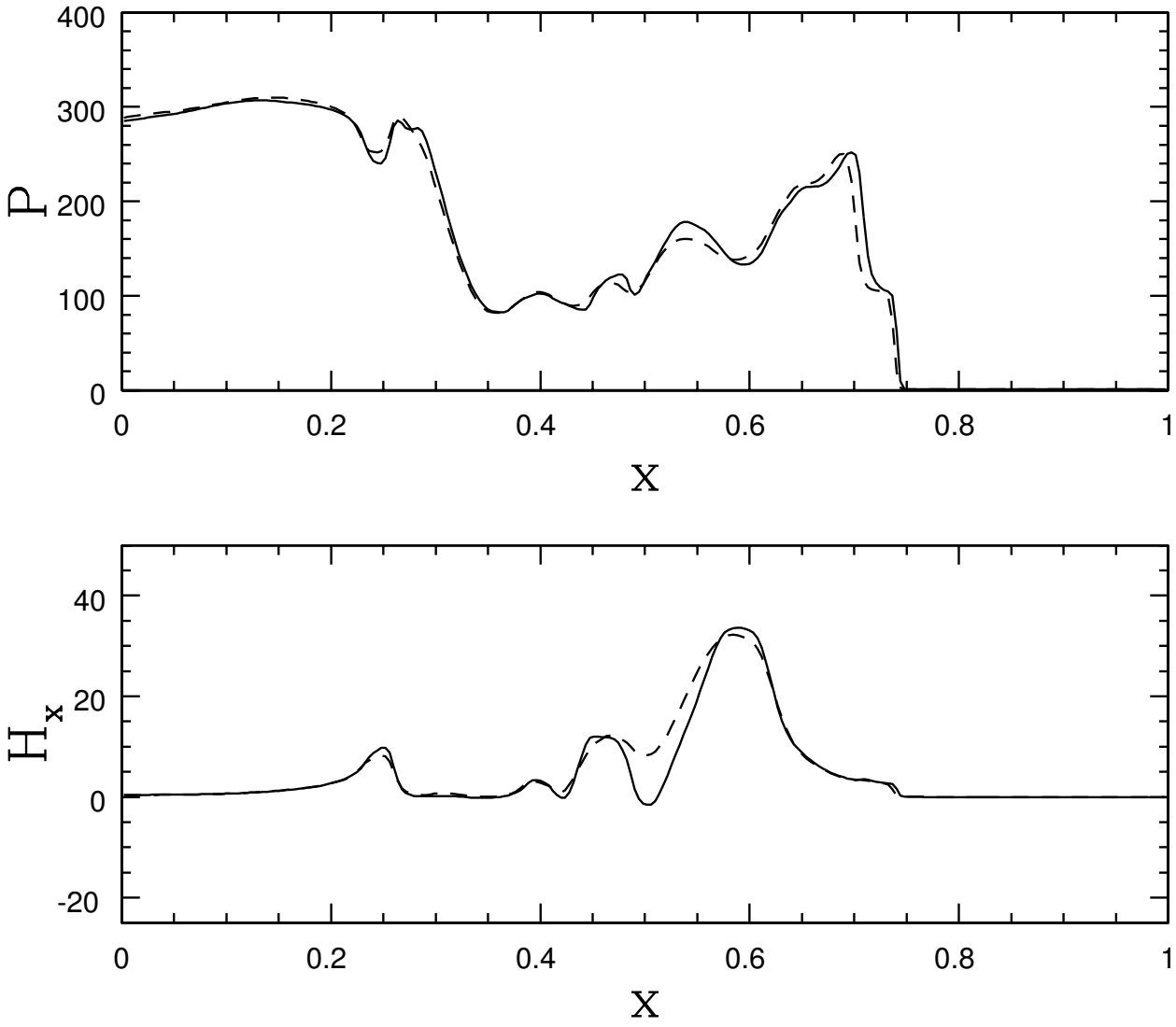

Figure A.10: Cut plots of thermal pressure (top) and the x-component of the magnetic field (bottom) for the magnetized cloud-shock problem taken at $t = 0.06$ at $y = 0.5410$. The solid curves are HSCD data and dashed curves are PLUTO data.